International Journal of Impact Engineering 177 (2023) 104592

Contents lists available at ScienceDirect

International Journal of Impact Engineering

journal homepage: www.elsevier.com/locate/ijimpeng

Modelling and optimisation of TPMS-based lattices subjected to high strain-rate impact loadings

Rafael Santiago [a,*], Henrique Ramos [a], Sara AlMahri [a], Omar Banabila [a], Haleimah Alabdouli [a], Dong-Wook Lee [a], Alia Aziz [a], Nitul Rajput [a], Marcilio Alves [b], Zhongwei Guan [a]

[a] Advanced Materials Research Center, Technology Innovation Institute, P.O. Box: 9639, Abu Dhabi, United Arab Emirates
[b] Department of Mechatronics and Mechanical Systems Engineering, University of São Paulo (USP), São Paulo, Brazil

ARTICLE INFO

Keywords:
Triply periodic minimal surfaces
Direct impact Hopkinson bar
Numerical modelling
Theoretical prediction
Strain-rate
Additive manufacturing

ABSTRACT

Lattices structures show promising applications in aerospace, biomedical and defence sectors, in which high energy absorption and lightweight structures are required. This work studies Triply Periodical Minimal Surfaces (TPMS) with potential for impact engineer applications, focusing on material characterisation, modelling and performance optimisation. For this purpose, stainless steel 316 L lattice samples made by additive manufacturing were tested in a wide range of strain-rates and various building directions using a universal testing machine and Split Hopkinson Pressure Bar, equipped with a Digital Image Correlation system. Then, the obtained properties were implemented in an explicit finite element model and validated against experimental results related to different TMPS topologies and impact scenarios. A theoretical model is also proposed to predict the TPMS-based lattices quasi-static and impact responses up to the densification threshold. Finally, the validated numerical models were used to predict the behaviour of several functionally graded TPMS topologies, indicating the architectures with superior impact performance. The graded topologies were then manufactured and experimentally tested. The results indicate that graded topologies exhibit up to 18% higher energy absorption when compared to their non-graded counterparts. The theoretical and numerical models developed in this paper provide an effective approach for designing and predicting high energy absorption architectures subjected to quasi-static and impact loadings.

1. Introduction

The use of lattice structures in engineered functional components has been growing recently due to additive manufacturing (AM) techniques. The AM techniques allow complex geometries to be produced by using polymers, metals and ceramics, which could not be otherwise made by traditional manufacturing techniques [1]. Lattice structures have brought attention to automotive, sport and defence applications due to their lightweight, tailored behaviour and high-impact energy absorption [2–5]. Furthermore, many researchers [3,6–9] have highlighted that the mechanical response of a lattice structure is governed by its material, architecture and relative density, which leads to endless possible combinations in designing and optimising such structures.

Lattice structures based on trusses have been explored under quasi-static and dynamic loading conditions [10–15], highlighting its bending-dominated mechanical response. However, recent studies on shell- and plate-based lattices have been proven to have high stiffness and impact energy absorbing capability [16–19]. Triply Periodic Minimal Surface (TPMS) architectures are shell-based lattices, defined by mathematical expressions, with an open cell and self-structured design, suitable for most AM techniques [5,8,20–23]. TPMS architectures present a primarily stretching-dominated mode of deformations, which lead to superior mechanical properties over truss-based lattices.

Modelling lattices under impact loadings is challenging due to their complex architectures, rate-dependant behaviour and the need for advanced explicit computational subroutines. Complex shapes demand highly-refined meshes, which leads to a long processing time and numerical instability. Karaov et al. [24] studied the collapse of truss-based lattices through both numerical and experimental approaches. Numerical models were developed based on the designed as well as re-constructed topology from X-ray computed tomography. The surface morphology influences the stress distribution of the lattices, inducing stress concentrations. However, the correlation between numerical and experimental results was poor. Complex architectures of truss-based

* Corresponding author.
E-mail address: rafael.santiago@tii.ae (R. Santiago).

https://doi.org/10.1016/j.ijimpeng.2023.104592
Received 1 August 2022; Received in revised form 2 March 2023; Accepted 28 March 2023
Available online 31 March 2023

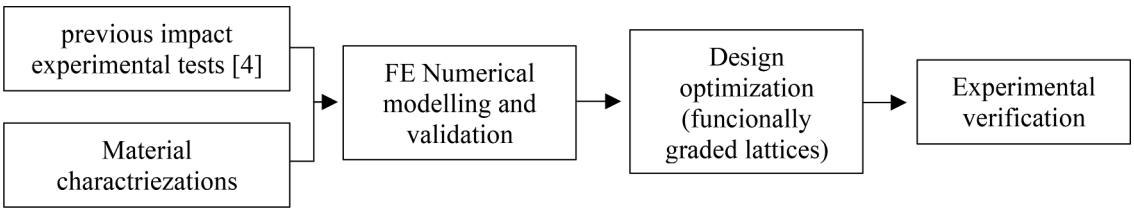

Fig. 1. Flow chart on the methodology used.

lattices were modelled by Lei et al. [25] and Smith et al. [26] using unidirectional truss elements in Abaqus/explicit, which provided predictions of the deformation mode of complex lattice architectures. Abueidda et al. [19] studied the compressive behaviour of TPMS made of polymeric material and predicted its elastic modulus and strength by using COMSOL. A good agreement was observed between the numerical and experimental results. Zhao et al. [27] studied Gyroid and Primitive TPMS topologies under compressive loading, with their mechanical response being predicted by using explicit finite element models. The model could also provide the prediction of the overall response of the lattice and its collapse mode; however, the study resulted in a poor prediction of the specific energy absorbed and stress level, with an error between 10 and 30%, depending on the lattice configuration. Wang et al. [28] explored the quasi-static compressive behaviour of cylindrical shells made by gyroid TPMS-based lattices. An explicit numerical model was developed using shell elements and bi-linear material models, with a good agreement between numerical and experimental data.

Li et al. [29] modelled TPMS structures made of 316 L stainless steel by selective laser melting. The material was characterised at strain-rates up to 190 $s^{-1,}$ with the failure modes observed under different triaxialities. An explicit finite element model was developed through the commercial code Abaqus with anisotropic material formulation for modelling a TPMS lattice. A good agreement with the experimental data was obtained. Peng et al. [30] modelled TPMS gyroid structures subjected to impulsive loadings by using simple planar elements, which was validated against the corresponding experimental data. The validated model was also used to predict the response of complex TPMS graded topologies. TPMS gyroids were also experimentaly and numerically studied under low velocity impact loadings by Ramos et al.[31]., tailoring its impact response by changing its isosurface formulation.

Although several structural lattice topologies can be proposed and manufactured in AM, their behaviour and applications are still not thoroughly studied, particularly when it comes to high strain-rate loading conditions. Once properly validated, numerical models are crucial to reduce the development time and cost and minimise the experimental work. However, there is no consensus on an appropriate methodology for modelling lattice structures that vary on element types, topology mapping, and material formulations. Moreover, those models can often result in unexpectedly good agreement with experimental results from simple formulations. Thus, modelling the impact response of lattice structures is still an open subject that needs to be appropriately explored and validated against experimental data.

In the authors' previous work, AlMahri et al. [4] developed an experimental study on TPMS-based lattices using the Direct Impact Hopkinson Bar (DIHB) apparatus. A comparative assessment of five different TPMS topologies (i.e., Gyroid, Primitive, IWP, Diamond and Fisher-Koch) was conducted, from quasi-static to 33 m/s impact loading regimen. The Diamond, Gyroid, and IWP topologies exhibited high specific energy absorption (SEA), which offers promising applications to resist impact and shock loadings with lightweight.

In the current work, Diamond, Primitive and IWP topologies were studied under static and dynamic loadings, aiming to enhance their impact performance. Here, the lattices made of 316 L stainless steel by additive manufacturing were mechanically characterised at a strain-rate up to 4000 s^{-1} using a universal testing machine and a Split Hopkinson Pressure Bar [32–34]. Then, explicit Finite Element (FE) models were developed, which were validated against the corresponding experimental results in a comprehensive set of impact scenarios. Finally, the validated FE model was used to design functionally graded Diamond architectures with enhanced impact performance, which were then experimentally verified.

Table 2
Selective laser melting manufacturing parameters used.

Equipment	EOS M290
Laser source	350 W, ytterbium fiber, single
Focus diameter	100μm
Chamber environment	Inert gas (nitrogen)
Build plate temperature	160 °C
Particle size	10–45 μm, gas atomised
Layer thickness	40 μm
Scanning strategy	Meander

2. Materials and methodology

The methodology used is shown in Fig. 1, which consists of initial material characterisation under quasi-static and dynamic strain-rates, using a universal testing machine (UTM) and a Split Hopkinson Pressure Bar (SHPB). Then, an explicit numerical model was developed and validated against the corresponding experimental data. Finally, various functionally graded lattice topologies were studied to optimise their impact performance, with the lattices being manufactured and experimentally verified under the impact condition.

The TPMS-based lattices studied here were made of 316 L stainless steel by laser powder-bed fusion (L-PBF) from gas-atomised powder. The chemical compositions and manufacturing parameters are listed in Tables 1 and 2. Material characterisation specimens were also made of the same material, following the same manufacturing procedure. All lattices and specimens were subjected to a post-heat treatment cycle of 600 °C for 2 h and 350 mBar in a vacuum furnace before they were extracted from a build platform.

2.1. Material characterisation

The tensile test specimens based on ASTM-E8 [35] and compressive samples, as shown in Fig. 2(a-b), were used to perform quasi-static and dynamic tests. Those samples were manufactured along the loading direction at the angles of 0°, 45° and 90° with the build chamber base,

Table 1
Compositions of stainless steel 316 L alloy.

Element	C	Si	Mn	Cr	Ni	Mo	P	S	Fe
%w	0–0.03	0–1	0–1	16–18	10–12	2–3	0–0.045	0–0.03	Balance

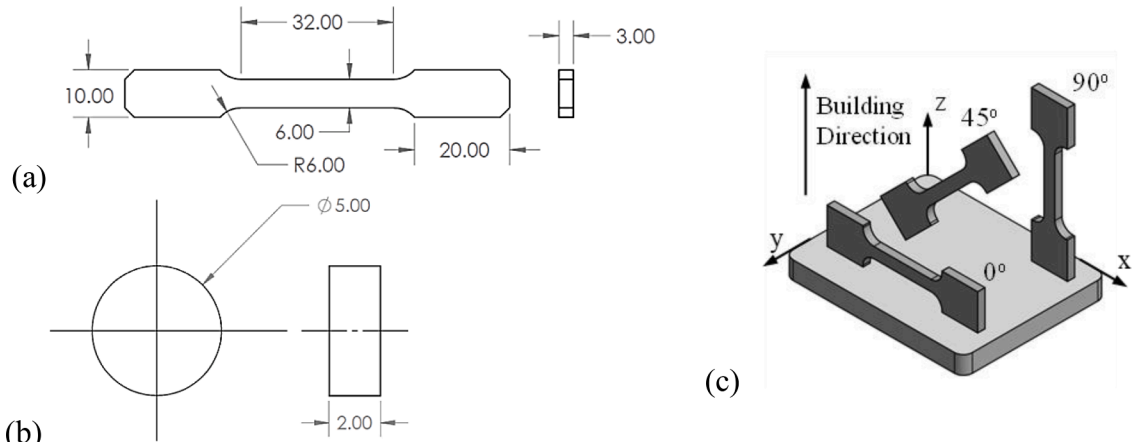

Fig. 2. (a) Tensile specimens based on ASTM-E8, (b) compressive specimens and (c) specimen distribution within the build chamber. (all dimensions in mm).

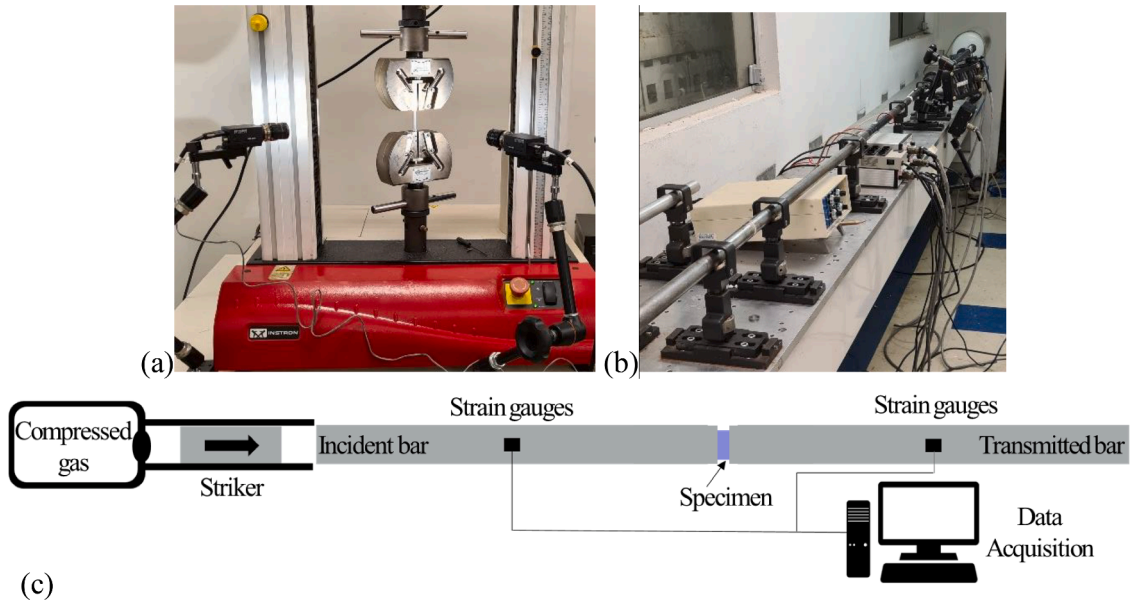

Fig. 3. (a) Universal testing machine and DIC, (b) SHPB used, and (c) SHPB scheme.

Fig. 2(c), to investigate the anisotropic behaviour resulted from the manufacturing process.

Tensile uniaxial tests were conducted in a universal testing machine Instron 3369 at a strain-rate of 0.003 s^{-1}, Fig. 3(a), with a 50 kN load cell. The strains in the specimen were monitored by a Digital Image Correlation (DIC) system (Correlated Solutions, VIC2D), covering the whole gauge length of the specimen up to high deformation levels [36]. Compressive tests were also performed at the same strain-rate and setup. The true material stress is defined as

$$\sigma_t = \frac{F}{A_0}(1+\varepsilon_1), \tag{1}$$

where F is the axial compressive/tensile force recorded by the load cell, A_0 is the initial cross-sectional area of the specimen and $\varepsilon_1 = \Delta l / l_0$ is the longitudinal engineering strain obtained from the DIC.

A scanning electron microscope (SEM) ThermoFisher Scientific, model Scios 2, was used to assess the fracture surface and microstructure of the printed samples. This system is integrated with an Electron backscattered diffraction (EBSD) model C-nano, made by Oxford Instruments, which was employed to evaluate the texture of the fabricated material. Here, an electron beam of 20–30 kV and a current of 1.6 nA was used, with a step size of 0.3–0.5 micrometers for mapping the sample. The texture and grain size analyses were performed using AZtecCrystal software. The material's sections through the xy-, xz- and yz-planes were cut and polished up to mirror-like finishing following metallographic procedures [37].

Dynamic compressive tests were performed using a Split Hopkinson Pressure Bar (SHPB) [32,34], in which a sample was placed between two metallic bars, as shown in Figs. 3(a) and (b). The incident and transmitted bars are made of SAE 1055 steel, with an elastic modulus of 193.91 GPa, a density of 7816.1 kg/m^3, 25 mm in diameter, and 2 m in length. A 250 mm long striker was used, accelerated by a compressed air reservoir attached to a high-speed discharge valve. The signal of the transmitted bar was recorded using a strain gauge (half-bridge), which was attached at the centre of each bar. The signals were then conditioned by a Fylde FE-H359-TA high-frequency strain amplifier and recorded by a National Instruments data acquisition PCI-6110 at 5 M samples/*sec*.

The test starts with the impact of the striker at the incident bar end, producing compressive pulse, $\varepsilon_i(t)$, that travels along the incident bar. Once the pulse reaches the end of the opposite bar, part of it passes through the sample and reaches the transmitted bar, $\varepsilon_t(t)$, and the remaining part is kept inside the incident bar, reflected as a tensile pulse, $\varepsilon_r(t)$. When the specimen equilibrium is reached, i.e. $\varepsilon_t(t) = \varepsilon_i(t) +$

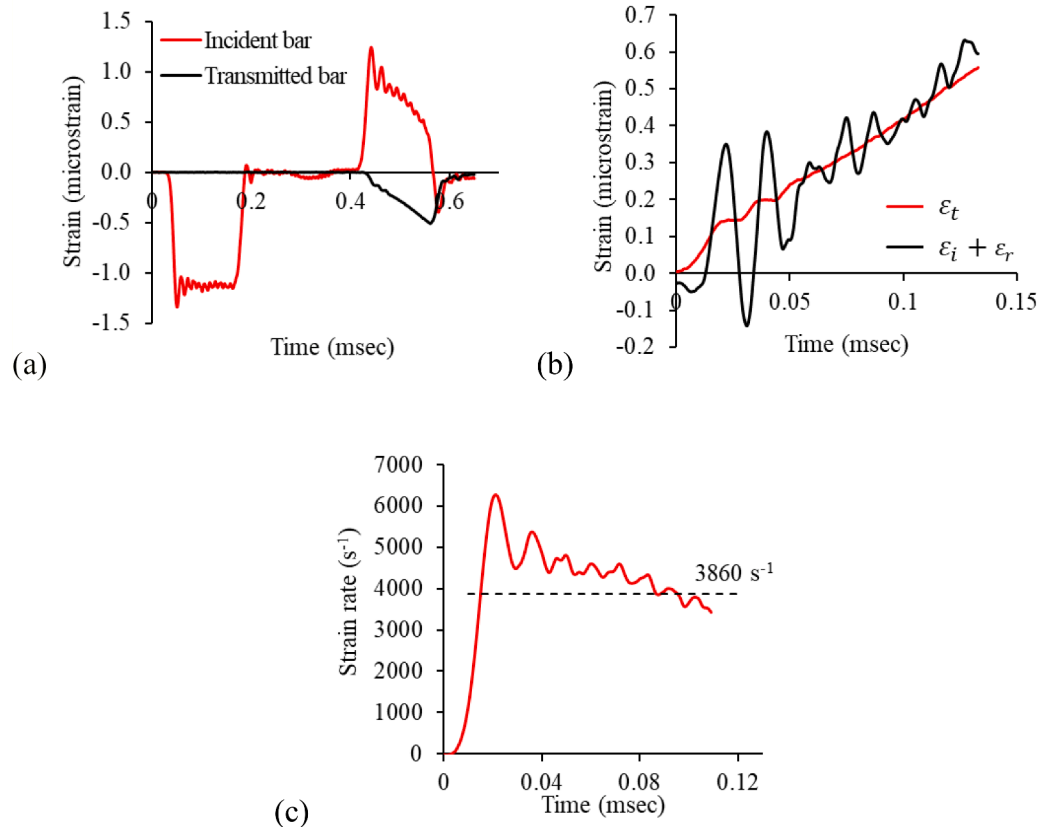

Fig. 4. Typical SHPB test results (a) strain-time history measured from the incident and transmitted bars in SHPB, (b) specimen equilibrium (c) strain-rate evolution during the test.

$\varepsilon_r(t)$, the deformation of the specimen, $\varepsilon_s(t)$, strain-rate, $\dot{\varepsilon}_s(t)$, and stress, $\sigma(t)$, are given as [38]

$$\varepsilon_s(t) = -\frac{2c_0}{l_s}\int_0^t \varepsilon_r(t)dt \tag{2}$$

$$\dot{\varepsilon}_s(t) = -\frac{2c_0}{l_s}\varepsilon_r(t) \tag{3}$$

$$\sigma(t) = E_B\frac{A_B}{A_s}\varepsilon_t(t) \tag{4}$$

where A_b and A_s are the cross-sectional areas of the bar and the spec-

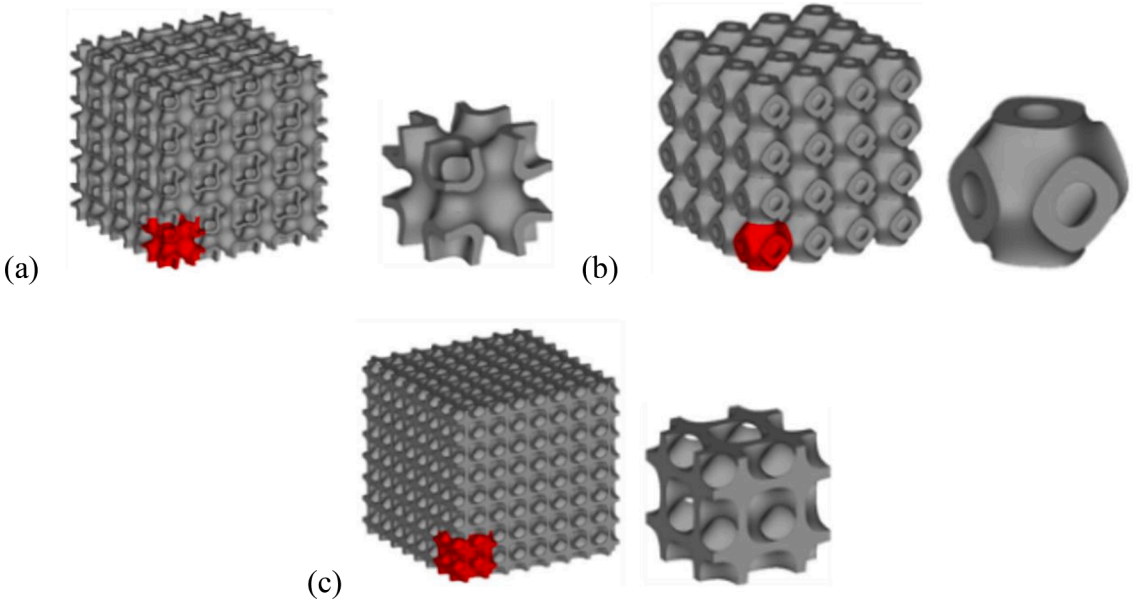

Fig. 5. TPMS unit cells and lattices designed: (a)Primitive (P), (b) IWP and (b) Diamond (D).

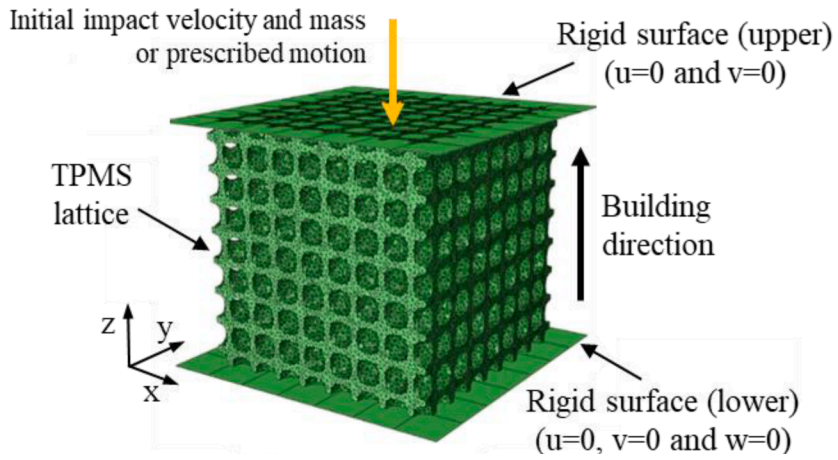

Fig. 6. Boundary constraints used for the FE lattice model developed.

imen, l_s is the specimen length, and $c_0 = \sqrt{E_b/\rho_b}$ is the elastic wave speed, given by the elastic modulus of the bar, E_b, and density, ρ_b. A time shift algorithm was used in MatLab to reduce the SHPB data, which was also used by Kariem et al. [34]. Fig. 4(a) shows a typical strain signal measured from SHPB, Fig. 4(b) presents the specimen equilibrium, and Fig. 4(c) shows the strain-rate evolution obtained from the tests.

2.2. Numerical modelling

Three TPMS topologies were numerically modelled in this study, namely Primitive (PR), IWP and Diamond (D). These topologies are described by the following mathematical surfaces [4,39]

$$\phi(x,y,z)_{Primitive} = \cos X + \cos Y + \cos Z \tag{5}$$

$$\phi(x,y,z)_{IWP} = 2(\cos X\cos Y + \cos Y\cos Z + \cos Z\cos X) - (cos2X + cos2Y + cos2Z) \tag{6}$$

$$\phi(x,y,z)_{Diamond} = \cos X\cos Y\cos Z - \sin X\sin Y\sin Z, \tag{7}$$

where $X = 2\alpha\pi x$, $Y = 2\beta\pi y$, and $Z = 2\gamma\pi z$ control the unit size in the *x-*, *y-*, and *z*-directions, for $\alpha = \beta = \gamma = 1$ and $\phi = 0$. Three relative densities ($\overline{\rho} = \rho_{Lattice}/\rho_{Solid}$) were used, replicating the configurations used in the experimental impact test developed previously [4]. The desired relative density was achieved by changing the wall thickness, *t*, offsetting the surface between $-t/2 \le \phi(x, y, z) \le t/2$. The modelled lattices consist of an array of 4 × 4 × 4 unit cells, resulting in a cubic lattice of 16 mm x 16 mm x 16 mm. The TPMS-based lattices unit cells are shown in Fig. 5. The effects of unit cell size have been explored by many authors [31,40–43], who have reported that, in general terms, unit cells from 4 × 4 × 4 and above are suggested to provide a suitable agreement to homogeneous behaviour. For example, according to Wang et al. (2021) [43], 4 × 4 × 4 unit cells give 5–8% result difference from TPMS lattices with a larger number of unit cells. Therefore, the unit cell size is kept the same for conducting this work, which provides a proper evaluation of the TPMS topology and the functionally graded lattices.

An explicit finite element (FE) model was developed through the commercial code Abaqus/Explicit, to model the whole 16 mm x 16 mm x 16 mm cube lattices and 4 × 4 × 4 unit cells with surface thickness according to the relative density defined. These lattices were input in the FE code Abaqus as a standard tessellation language (.stl) format and then meshed using 10-noded tetrahedral elements C3D10M, with second-order formulations and hourglass control [44].

The lattice was modelled between two rigid surfaces, as shown in Fig. 6. The upper surface can only move along the *z*-direction, in which the impact mass and velocity are defined, or the prescribed movement in a quasi-static loading case. The lower surface is fully fixed, with surface-to-surface contact being defined for all the possible interactions between the lattice and the top face of the bottom rigid plate.

The dynamic compressive events were modelled using a mass of 0.55 kg at an impact velocity of 33 m/s, following the DIHB conditions reported by AlMahri et al. [4]. The quasi-static tests were modelled with an upper surface moving downward at a displacement rate of 1 mm/min up to a complete densification of the lattice. Mesh sensitivity analysis was performed, covering element sizes from 1 mm down to 0.1 mm. It was identified that a mesh size of 0.3 mm resulted in a balanced solution between the accurate simulation results and CPU time consumption, as shown in Appendix A.

The Hill's Yield Criterion [45–48] anisotropic yield law was used for modelling the AM stainless steel 316 L behaviour. The material stress response aligned with the x-axis was taken as a reference for material direction ($\theta = 0^o$) and for the equivalent isotropic yield stress ($\overline{\sigma}_0$). Thus, the anisotropic yield limit is expressed as

$$\mathrm{F}(\sigma_{yy} - \sigma_{zz})^2 + G(\sigma_{zz} - \sigma_{xx})^2 + H(\sigma_{xx} - \sigma_{yy})^2 + \\ +2L\sigma_{yz}^2 + 2M\sigma_{zx}^2 + 2N\sigma_{xy}^2 = \overline{\sigma}_0^2, \tag{8}$$

where F, G, H, L, M and N are independent anisotropic constants estimated from the experimental tests using the approach presented by Neto et al. [47] and Jweeg et al. [48]. Once the tensile samples were loaded on the x-z plane, σ_{yz} and σ_{xy} were assumed isotropic, with $L = N = 1.5$ being considered in Hill' formulation. Assuming that the tensile specimens are in the plane stress condition ($\sigma_{yy} = \sigma_{yz} = \sigma_{xy} = 0$) and subjected to uniaxial loading (Fig. 2c), σ_θ, the transformation of the yield stress components are given by

$$\begin{cases} \sigma_{xx} = \sigma_\theta \cos^2\theta \\ \sigma_{zz} = \sigma_\theta \sin^2\theta \\ \sigma_{zx} = \sigma_\theta \sin\theta\cos\theta \end{cases} \tag{9}$$

resulting in a uniaxial yield stress $\overline{\sigma}_\theta$ deined as

$$\overline{\sigma}_\theta = \frac{\overline{\sigma}_0}{\sqrt{F\sin^4\theta + G\cos^4\theta + H\cos^2 2\theta + 2N\sin^2\theta\cos^2\theta}}. \tag{10}$$

The anisotropic parameters of F, G, H and N were identified based on the experimental test. The procedure was based on an optimisation algorithm developed in Matlab to minimise the error function between experimental and predicted yield stresses. The error function is defined as

$$error = \sum \left(\overline{\sigma}_\theta^{Hill} - \overline{\sigma}_\theta^{Exp}\right)^2. \tag{11}$$

with $\theta = 0°$, $45°$ and $90°$.

In addition to the anisotropic yield formulation, a tabled material plastic response was included with strain-rate hardening effect, $\kappa_{\dot{\varepsilon}}$, taking the mathematical form by Johnson and Cook [49,50] as

$$\kappa_{\dot{\varepsilon}} = \left[1 + C ln\left(\frac{\dot{\varepsilon}}{\dot{\varepsilon}^{ref}}\right)\right], \tag{12}$$

in which $\dot{\varepsilon}$ is plastic strain-rate and the reference strain-rate is $\dot{\varepsilon}^{ref}$=0.001s^{-1}. Ductile damage and evolution [51] were implemented in the FE modelling. For this, the damage initiation strain, ε_D^{pl}, was defined as an average onset of damage strains observed in the material strain-stress response, and the element failure displacement, δ_f, estimated by the average of element size and maximum strain obtained from the experimental data.

2.3. Theoretical modelling

The average plateau stress level, plateau slope and densification limit of TPMS-based lattices during the quasi-static and impact loadings were predicted by adopting the Gibson's cellular theory [3,52], combined with the Johnson and Cook strain-rate hardening, as

$$\frac{\overline{\sigma}}{\sigma_y} = c_2 \overline{\rho}^{n_2} \kappa_{\dot{\varepsilon}}, \tag{13}$$

where $\overline{\sigma}$ is the average plateaus stress, σ_y is the yield stress of the base material, c_2 and n_2 are exponential parameters related to the topology and boundary conditions of the lattices, extracted from quasi-static tests. The TPMS strain-rate was estimated as $\dot{\varepsilon} = kV_{imp}/h$, given the impact velocity, V_{imp}, the lattice cube height, h, and k, which is the strain-rate attenuation of the strain-rate subjected to the base material and the overall strain-rate applied to the lattice cube.

The plateau slope, $\overline{E}$, and densification limit, $\overline{\sigma}_d$, were also predicted by the following relationships as

$$\frac{\overline{E}}{E_p} = c_3 \overline{\rho}^{n_3}, \tag{14}$$

$$\frac{\overline{\sigma}_d}{\sigma_y} = c_4 \overline{\rho}^{n_4}, \tag{15}$$

where E_p is the plastic modulus of the base material, and the constants, c_3, c_4, n_2, n_4 are obtained from quasi-static compressive tests of TPMS, depending on the topology and boundary conditions.

2.4. Evaluation of functionally graded TPMS

Comparative numerical studies were carried out by proposing eight different unidirectional functionally graded D TPMS-based lattices and comparing its impact performance to a non-graded D topology. The lattices were 16 mm x 16 mm x 16 mm cubes, with 4 × 4 × 4 unit cell, 30% overall relative density, with the boundary constraints being described in Section 2.2. The scope of this evaluation was to propose functionally graded topologies by fixing the unit cell size, TPMS type, lattice cube size and overall relative density, with only the lattice wall thickness being changed according to the chosen graded functions. These functionally graded lattices can be easily implemented in any TPMS lattices designed by surface shifting, which motivates the proposed approach. The proposed relative density gradients used are described in Section 3.3, being its impact behaviour compared with a baseline configuration in terms of deformation after impact (DAI), and specific energy absorption (SEA), which is defined as:

$$\text{SEA} = \frac{EA}{m} = \frac{1}{m}\int F d\delta \tag{16}$$

where F is compressive force, δ is the lattice displacement, m is the lattice mass, and EA is the energy absorbed, given by the area under the load-displacement curve.

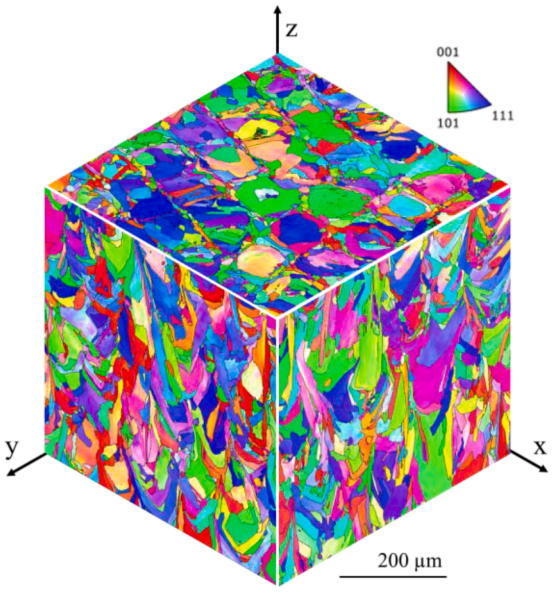

Fig. 7. Resulting materials microstructure texture on the xy-, xz and zy-planes.

2.5. Verification tests

Once the functionally graded TPMS topologies were numerically modelled, the most promising topologies were additively manufactured by L-PBF, as described in Section 2. The lattices were tested using a Direct Impact Hopkinson Bar (DIHB) to verify the numerical modelling outputs. DIHB is an impact device which can apply an impact compressive loading up to the complete densification of a material. The device is formed by pneumatic launcher, impact striker, and a 25 mm diameter transmitted bar, which can accommodate the entire TPMS lattice cube faces tested. The same experimental setup has been used in Almahi et al. [4], in which more details can be found. The impact verification was evaluated against the functionally graded and their non-graded counterparts in terms of deformation mode, SEA and DAI, with three tests being performed for each topology to confirm its repeatability.

3. Results and discussion

3.1. Mechanical characterisation

The microstructure texture analysis of the material sample was carried out using the EBSD mapping, Fig. 7 and Appendix B. The laser scan lines and the melt pools can be observed in the microstructures, with the grain following this pattern. The evaluation of the yz- and xz-planes do not indicate a specific preferred orientation of the grain; however, the mapping obtained from the xy-plane shows a minor preference along the ⟨110⟩ orientation. The grain distribution indicates the presence of a few hundreds of nm to hundreds of microns dominating in the range of 30–50 µm size (equivalent diameter).

Three repeated tensile tests were performed for each of 0°, 45° and 90° printing directions, with the samples being failed within the specimen effective gauge length, as shown in Fig. 8. The SEM images of fracture surfaces and the stress-strain responses are shown in Figs. 9 and 10, respectively.

The ductile behaviour was observed in all the directions tested, with an evident elastic and plastic regimes and a clear yielding, Fig. 10. In addition, the specimens showed a slight necking before the rupture, with a cup and cone formation, which suggests a ductile-dominant failure mode. The SEM images, exhibited in Fig. 9(a) and (b) show details of the

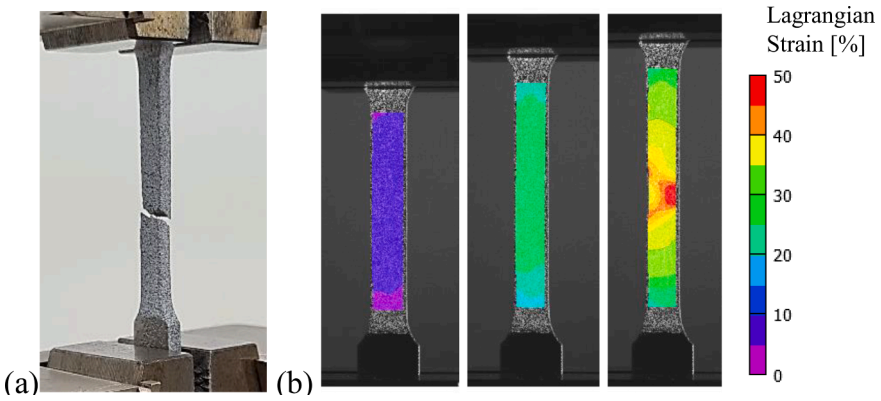

Fig. 8. (a) Tensile specimens after the test and (b) DIC strain field measurements of tensile test samples.

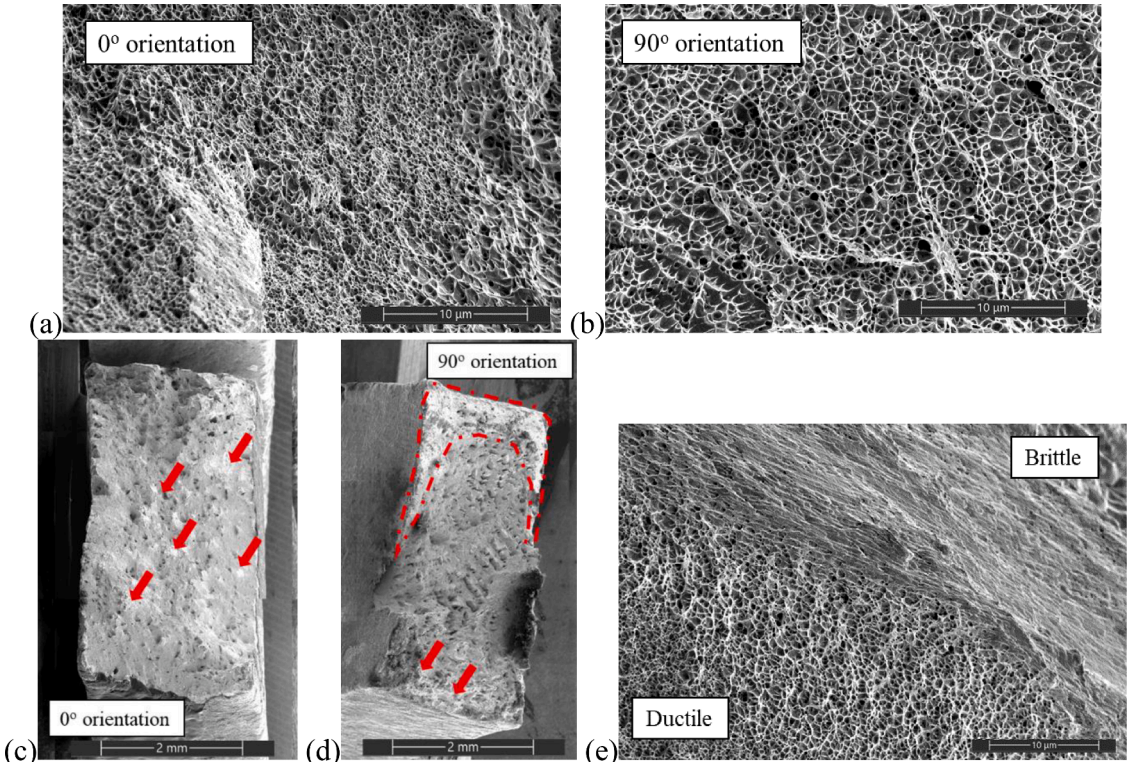

Fig. 9. SEM images of the fracture surface: (a-b) comparison of the sizes of the dimples on 0° and 90° samples, (c-d) comparison of ductile and brittle failure modes (brittle fracture highlighted); and (e) visualisation of ductile and brittle fracture mode transition.

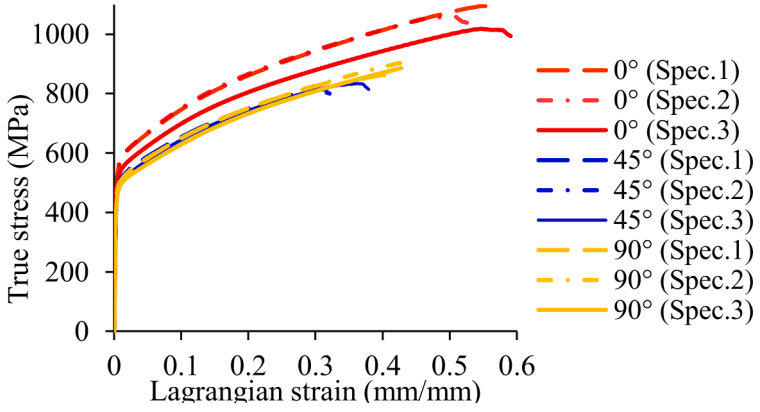

Fig. 10. Lagrangian strain and true stress of stainless steel 316 L samples manufactured at different directions.

Table 3
Material properties obtained from the material characterisation tests.

Building Direction	E (GPa)	ϑ	σ_f (MPa)	ε_f (mm/mm)	$\bar{\sigma}_\theta$ (MPa)
0°	155 ±70	0.33 ±0.01	1044 ±51	0.57±0.04	493 ±49
45°	115 ±60	0.35 ±0.01	793±10	0.33±0.05	465 ±12
90°	146 ±24	0.33 ±0.02	864±28	0.39±0.07	462 ±25

fracture surface, in which a clear formation of dimples can be observed at 0° and 90° samples, corroborating a ductile behaviour.

An evident difference was noted between the plastic regimes obtained from the samples manufactured at 0° and 90°. A higher plastic behaviour was observed for the samples that were loaded aligned to the deposited layers formed during the manufacturing (0° samples), with lower plasticity stresses when the material was loaded with an angle to the deposited layers (45° and 90° samples). In those cases, the difference between the plastic stresses obtained from the samples loaded at 0° and 90° varies from 13% to 15%. It indicates that the formed layers and the resulting microstructure influence the plastic regime of the material. The difference between the dimple sizes on the samples manufactured at 0° and 90° can be noted by comparing Fig. 9(a) and (b), which highlights the differences in the grain sizes, which also agrees with the microstructure evaluation.

The microstructure texture (EBSD) also points to a minor anisotropy of the resulting alloy, with the anisotropic response being evident from the strain-stress curves. Despite of the existence of anisotropy, it seems that the degree of anisotropy observed in the microstructure is smaller than those reported in other studies for the same alloy made by L-PBF. Here, the difference of yield stresses in 0° and 90° directions is between 50 and 70 MPa, smaller than the difference up to 210 MPa reported in other studies [53–55]. This suggests that the manufacturing technique and post-processing used here could reduce, but not eliminate, the resulting anisotropy of the alloy.

Anisotropic effects were also noted on the failure strain, ε_f, of the specimen manufactured in different directions. A ductile dominant fracture surface was observed in Fig. 9(c)-(d), with minor spots of cleavages resulted from brittle failure, Fig. 9(e). As shown in Fig. 10, the specimen loaded in the direction of the deposited layers (0° samples) exhibited a larger failure strain in comparison to the ones perpendicularly loaded (90° samples). It is also evident by comparing Fig. 9(c) and (d) that a large amount of brittle failure can be seen on 90° samples.

The specimen manufactured at 45° exhibited an even lower failure strain, Fig. 10. However, it is important to emphasise that the 45° samples have the maximum shear plane aligned to the material deposition layers, which indicates that the deposited layers can prematurely trigger the material shear failure. Furthermore, the failure strain of the material show a difference of up to 40% according to the specimen built-up direction, which indicates that the formed layers and the resulting microstructures influence the material behaviour. Table 3 summarises elastic modulus, E, Poisson ration, ϑ, ultimate stress, σ_f, and ultimate strain, ε_f of the material.

The SHPB results are summarised in Fig. 11(a)-(c), in which the material compressive responses can be observed at a quasi-static loading rate and strain-rates of 2000 - 4000 s^{-1}. A strain-rate hardening can also be observed for all the material build-up directions, but with higher

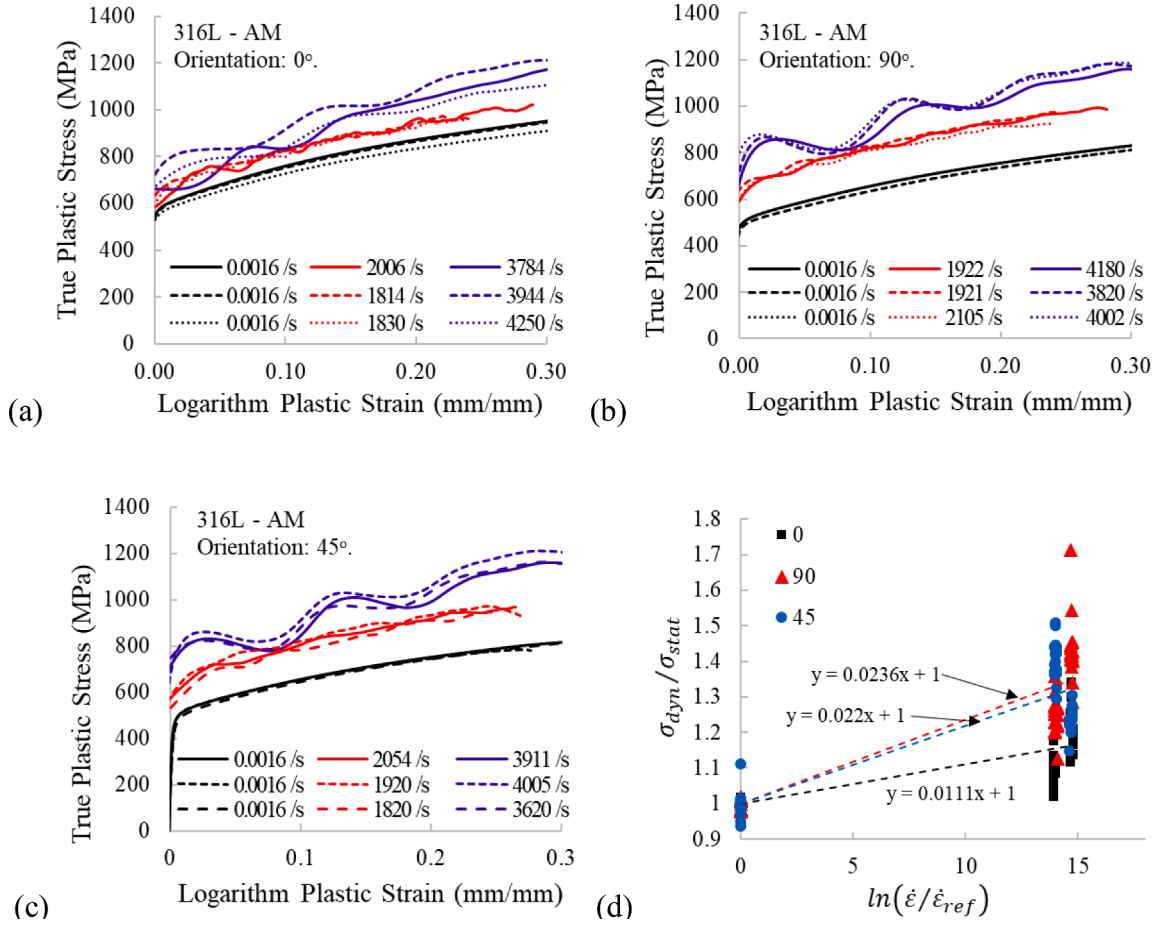

Fig. 11. Quasi-static and dynamic behaviour of 316 L stainless steel made by additive manufacturing when loaded at (a) 0°, (b) 90° and (c) 45° with the build chamber base. (d) Material dynamic hardening.

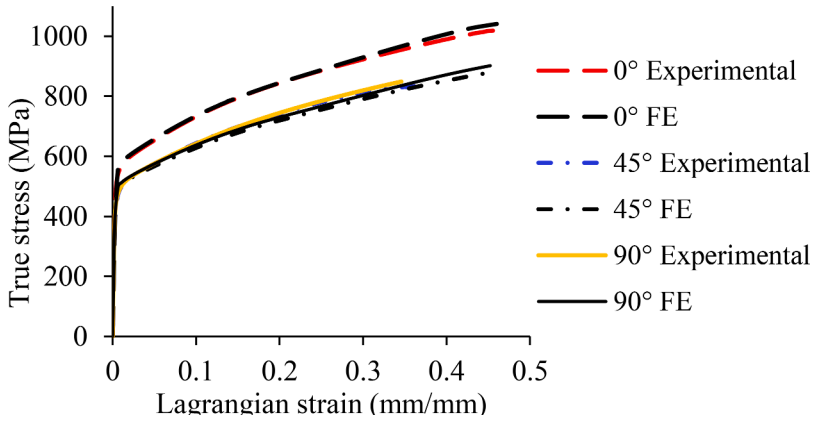

Fig. 12. Numerical and experimental material response stainless steel 316 L response made by additive manufacturing. The finite element model developed captured the anisotropic behaviour.

Table 4
Summary of the material parameters used, being ϵ_f the fracture strain and **η** the stress triaxiality.

E (GPa)	ϑ	C	ϵ_f (mm/mm)	η	δ_f(mm)
138.00	0.34	0.0190	0.42	0.33	0.13
F	*G*	*H*	*L*	*M*	*N*
0.7246	0.5828	0.4172	1.5993	1.5000	1.5000

strain-rate sensitivity for 45° and 90°, in comparison to 0° samples (Fig. 11(d)).

3.2. Numerical validation

Tensile dog-bone specimens (Fig. 2(a)) were numerically modelled as shown in Fig. 12, with anisotropic response being taken into account. Clearly, a good agreement between the experimental and predicted true stress – Lagrangian strain relationships was obtained. The constitutive parameters used in the modelling are summarised in Table 4.

The TPMS FE models were validated against the experimental data from the quasi-static and dynamic compressive tests as reported in reference [4] for the TPMS cube lattices studied. Fig. 13 presents the comparisons of the experimental and numerical deformation modes of the TPMS. The evolution of the deformation for lattice D is shown in Fig. 14 when loaded in static and dynamic loading regimes. The reasonable agreement between numerical and experimental results for all the scenarios is evident. The compressive load is uniformly applied to all the lattice layers through the specimen height direction, with a visible lateral expansion observed at high deformation levels (`barrel--shaped`) due to Poisson's ratio effect. The FE also captured the shear-dominated deformation mechanism, formed by diagonal shear deformations when the lattices reach the plateau stage.

No fracture failure, fragmentation, or spalls were observed from both the FE simulations and experimental results. The simulation captures the overall deformation pattern well, in comparison to the experimental

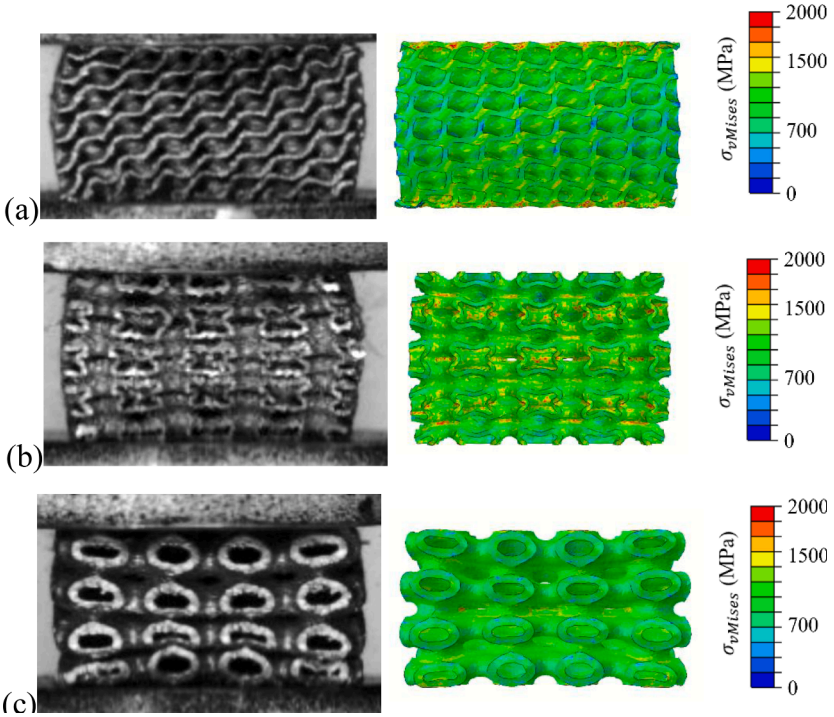

Fig. 13. Numerical and experimental comparison of (a) Diamond 27% relative density, (b) IWP 28% relative density and (c) Primitive 27% relative density, loaded at $t = 0.022$ *ms*.

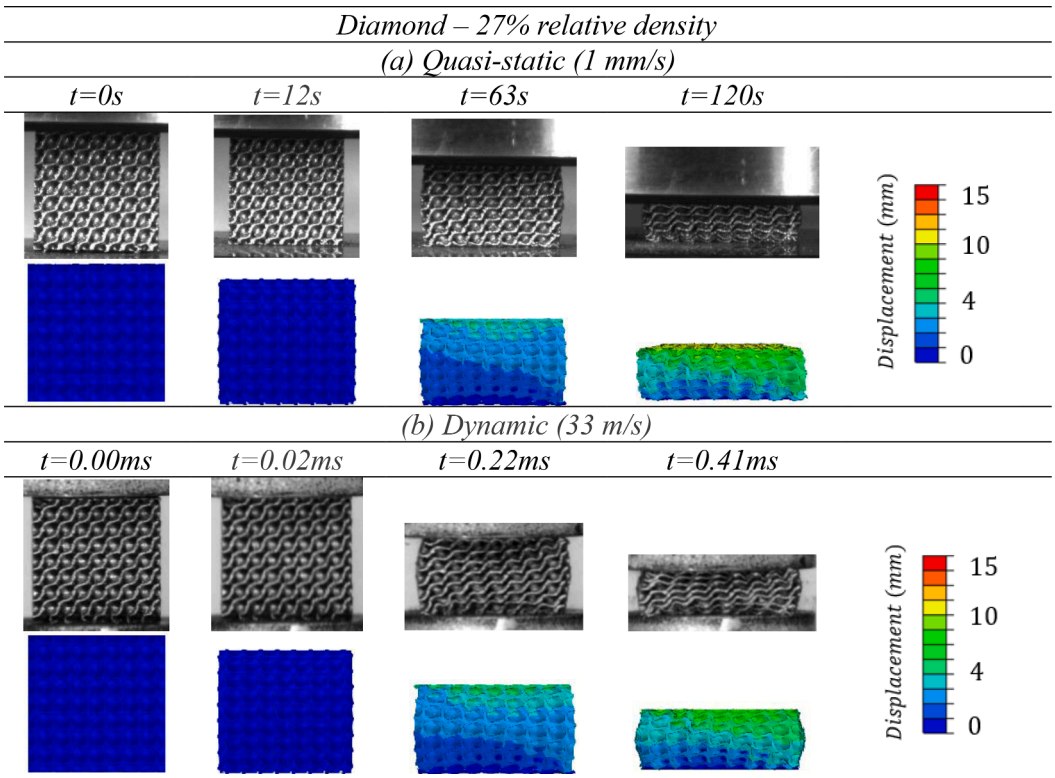

Fig. 14. Comparison of the evolution of the deformation mode comparison for Diamond lattice under (a) static and (b) dynamic loadings.

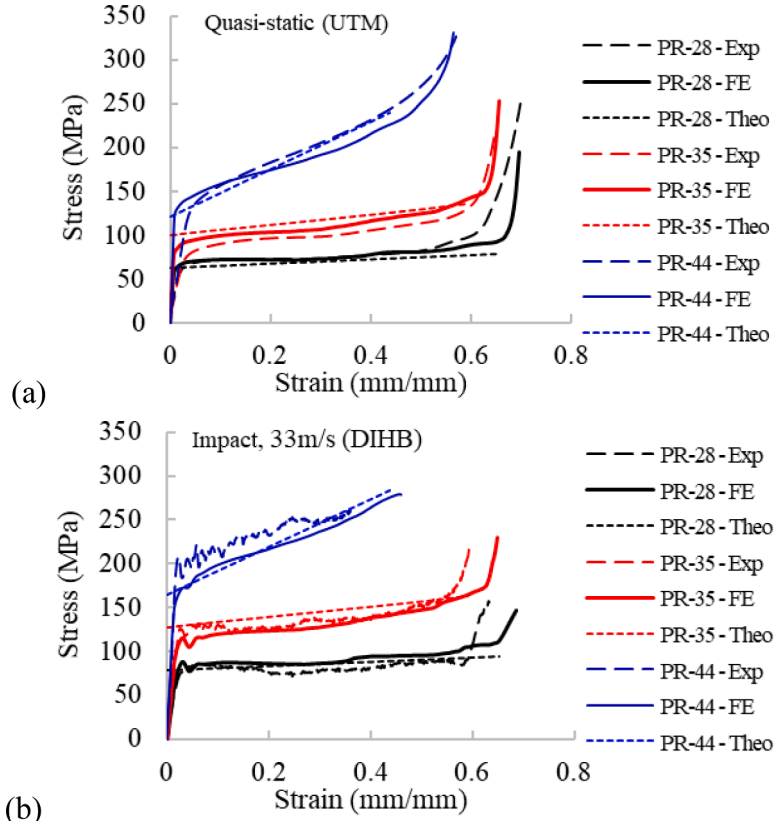

Fig. 15. Numerical and experimental comparison of Primitive TPMS topology loading at (a) quasi-static and (b) dynamic strain-rates.

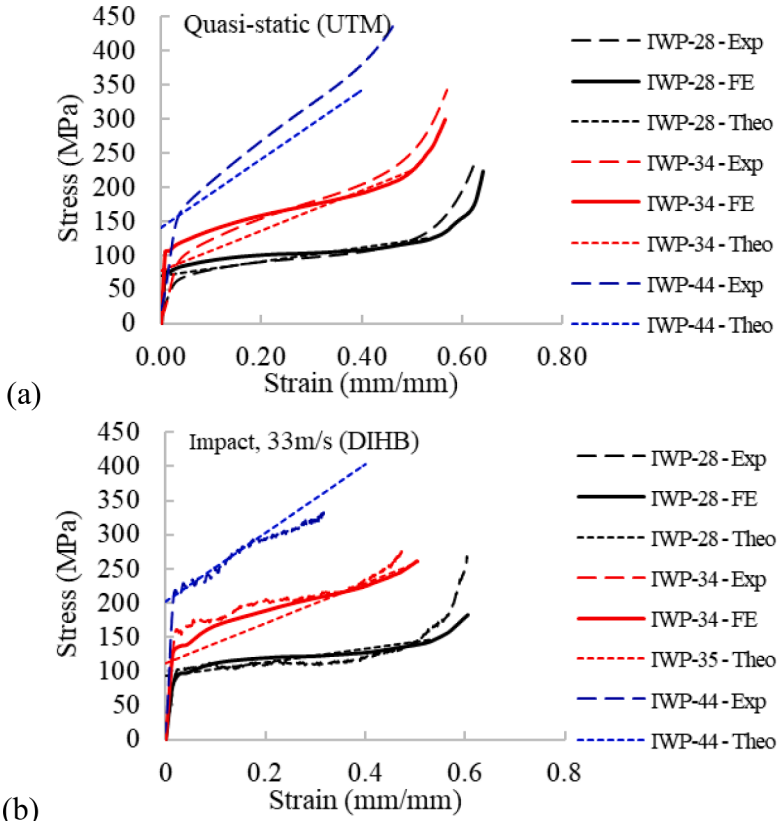

Fig. 16. Numerical and experimental comparison of IWP TPMS topology loading at (a) quasi-static and (b) dynamic strain-rates.

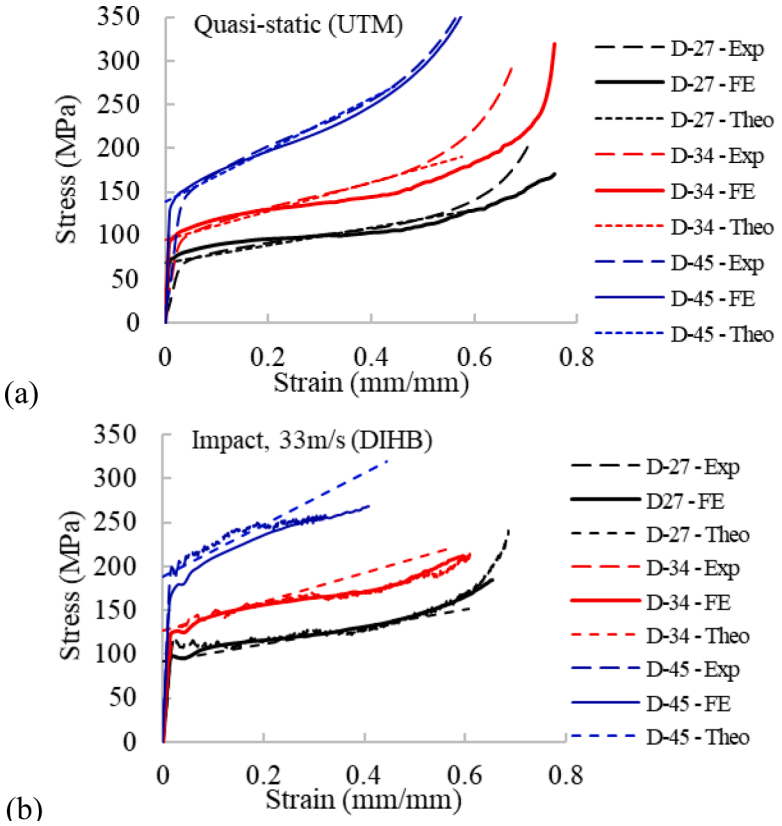

Fig. 17. Numerical and experimental comparison of Diamond TPMS topology loading at (a) quasi-static and (b) dynamic strain-rates.

Table 5
Quantitative comparison of plateau stress (PS) and specific energy absorption (SEA) for the lattices modelled.

Topology – Rel. Dens. (%)	Loading Rate	PS Exp.* (MPa)	PS FE[1] (MPa)	Error (%)	SEA. ** (J/g)	SEA FE** (J/g)	Error (%)
PR-27%	Static	74.88	74.08	-1.07	16.89	17.05	0.93
PR-27%	Dynamic	79.71	85.75	7.58	14.42	15.67	8.67
PR-35%	Static	98.84	108.06	9.33	22.62	24.09	6.51
PR-35%	Dynamic	128.50	122.55	-4.63	23.44	22.68	-3.24
PR-44%	Static	197.93	204.31	3.22	43.94	43.26	-1.56
PR-44%	Dynamic	233.92	215.35	-7.94	37.69	35.12	-6.84
IWP-28%	Static	94.88	102.97	8.53	22.31	23.16	3.84
IWP-28%	Dynamic	108.60	116.79	7.54	20.30	21.21	4.52
IWP-34%	Static	172.73	171.30	-0.83	37.46	38.48	2.72
IWP-34%	Dynamic	194.94	184.25	-5.48	35.61	34.32	-3.63
D-27%	Static	98.05	98.46	0.42	21.64	22.45	3.74
D-27%	Dynamic	112.27	113.64	1.22	21.29	20.90	-1.83
D-34%	Static	142.52	135.41	-4.99	31.46	30.73	-2.31
D-34%	Dynamic	155.24	152.84	-1.55	27.23	28.49	4.61
D-45%	Static	221.76	218.51	-1.47	48.59	49.07	0.99
D-45%	Dynamic	242.06	229.65	-5.13	34.59	32.60	-5.75

* : The average of $0.05 < \varepsilon < 0.40$.
** : Up to $\varepsilon = 0.50$ for static, and $\varepsilon = 0.40$ for dynamic.

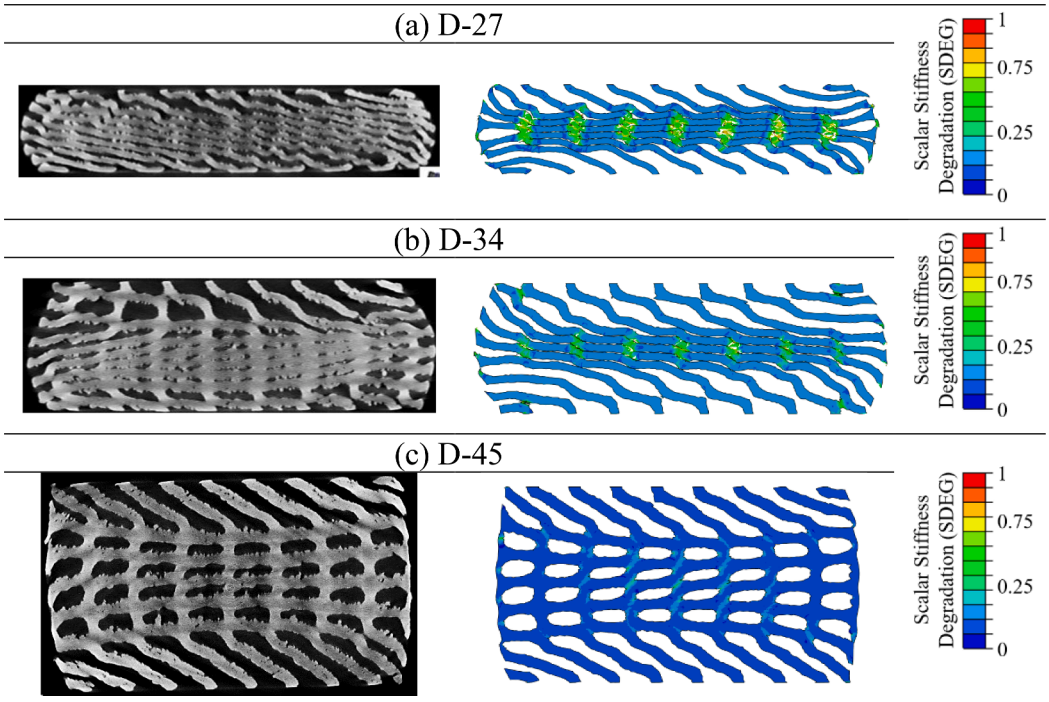

Fig. 18. Comparison of x-ray CT images and FE for (a) D-27, (b) D-34 and (c) D-45. Consistent prediction of the lattices deformation mode and densification prediction.

observations for all the TPMS-based lattices studied.

The simulated stress-strain responses of lattices subjected to quasi-static and dynamic loading conditions are presented in Figs. 15–17, together with the experimental data for better comparisons. It is evident that the FE modelling captures the initial elastic stage, followed by the plateau formation and the densification stage for all TMPS topologies tested experimentally. A good agreement between the numerical and experimental curves was obtained until the end of plateau stage, with some deviations after the densification. This is likely due to geometrical and material imperfections, surface roughness and friction between the lattice cells, which are not considered in the FE modelling.

Table 5 summarises testing results for TPMS-based lattices studied, together with the experimental results. The plateau stress (PS) was extracted as average stress between the strains of 0.05 mm/mm and 0.40 mm/mm, whereas the SEA was obtained up to the strain of 0.50 mm/mm and 0.40 mm/mm, for the static and dynamic tests, respectively. A small discrepancy between the numerical and experimental results was noted as 4.43% for PS and 3.86% for SEA on average. The strain-rate hardening was also noted from the FE results, as previously observed in the experimental results [4].

The X-ray Computed Tomography (CT) images and FE predictions of D-27, D-34 and D-45 after the impact are shown in Fig. 18. The FE modelling provides the prediction of the internal densification of the lattice in accordance with that observed experimentally. The CT and FE images show the shear band deformation mode and the homogenous loading along the height. The FE modelling also captures the crack initiation location, as highlighted in Fig. 19. Those places are mainly located in the vertical connections between unit cells, which seems

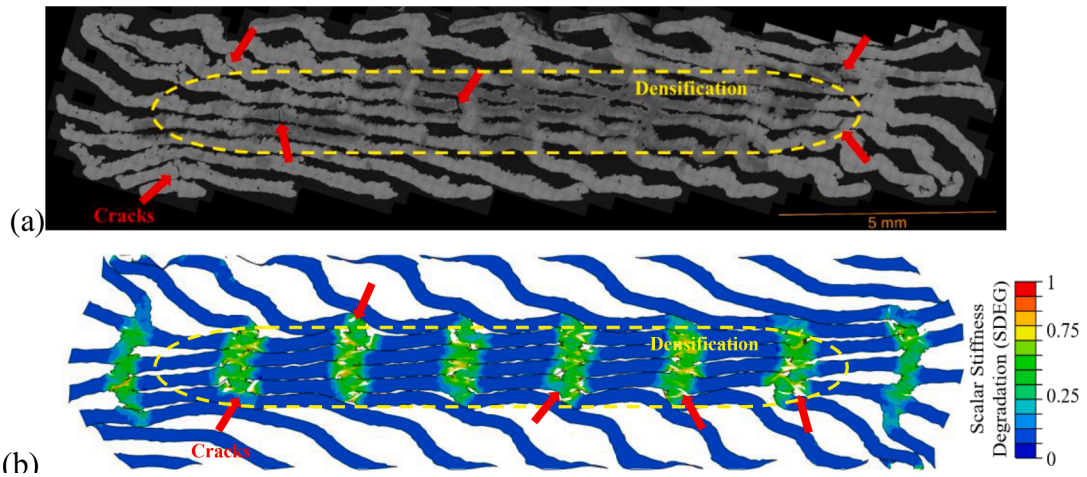

Fig. 19. Comparison of the post-impact cross-section of Diamond 27% relative density lattice: (a) experimental and (b) numerical.

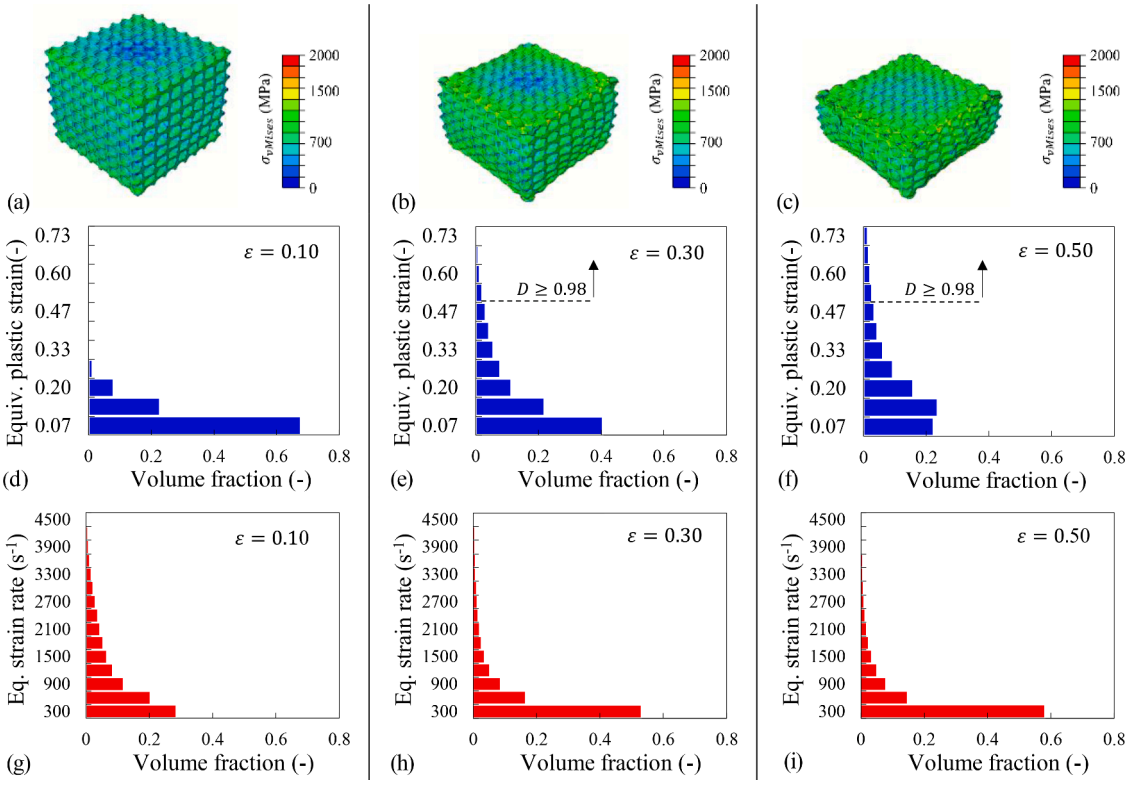

Fig. 20. Analysis of the deformation response of D type TPMS. Contour plot of the von Mises stress for (a) 0.1, (b) 0.3 and (c) 0.5 lattice compressive strain. (d)-(f) Equivalent plastic strain histogram during impact. The majority of the elements loaded below the material fracture strain. (g)-(i)Strain-rate histogram during impact. The majority of the elements loaded below 2000 s^{-1} and no elements loaded beyond 4000 s^{-1}.

attributed to the concentrated bending and buckling loadings. The formation of those cracks triggers the collapse of lattice, most evidente during the plateau stage. Additionally, densification occurs inside the lattices, not apparent in the peripheral regions.

Figs. 17(b) and 18 suggest that the plateau formation is related to the densification of the lattices, once the D-27 and D-34 lattices exhibit a clear plateau formation and evident internal densification, not observed in D-45 though. Thus, the plateau formation is due to the densification and collapse of the unit cells.

The evolution of the equivalent plastic deformation accumulated by the elements is presented in Figs. 20(d) and 20(f) for three compressive strain levels during impact (Fig. 20(a)–(c)). It is noted that 87% of the elements are in the plastic regime, which corroborates the high-energy absorption capability observed in this topology. However, it is worth noting that 45% of the elements are subjected up to 13% of plastic strain, and 25% of the elements are subjected up to only 6% of plastic strain. Thus, although relatively high SEA is observed for these lattices, the TPMS shows potential for further improving its impact energy-absorbing capability.

Figs. 20(g) and 20(i) present the strain-rate histogram during the 33 m/s impact, which subjected the TPMS to an overall strain-rate of 2057 s^{-1}. The histograms show that the strain-rate reduces as the TPMS deforms and absorbs the impact energy. A significant percentage of the elements (45.2%) is subjected to a 600 s^{-1} strain-rate or less, and only

Table 6
Theoretical experimental parameters.

Topology	c_2	n_2	(R^2)	c_3	n_3	(R^2)	c_4	n_4	(R^2)
D	1.4376	1.5766	(0.9967)	1.6167	2.1255	(0.9945)	1.7095	1.4245	(0.9945)
PR	1.9087	2.0274	(0.9622)	13.9447	4.9259	(0.9977)	3.0734	2.2840	(0.9977)
IWP	3.1106	2.2155	(0.9519)	9.5572	3.4585	(0.9709)	4.2631	2.1813	(0.9709)

Table 7
Summary of theoretical SEA for the TPMS studied under quasi-static and impact loadings.

Topology	Relative Density	Theoretical SEA (J/g) 5 mm/min (quasi-static)	33 m/s (impact)	Dynamic enhancement (%)
D	0.27	28.08	34.26	+22.0
D	0.34	37.97	46.37	+22.1
D	0.45	41.99	52.07	+24.0
PR	0.27	21.21	26.09	+23.0
PR	0.35	32.10	39.57	+23.3
PR	0.44	36.65	45.48	+24.1
IWP	0.28	23.34	28.67	+22.8
IWP	0.34	34.06	41.78	+22.6
IWP	0.44	42.44	53.15	+25.2

1.5% of the elements are loaded between 1200 s^{-1} and 2400 s^{-1}. It shows that the strain-rate subjected to the base material is about 3 times less than the overall strain-rate applied to the cubic lattices ($k \sim 3$).

3.3. Theoretical predictions

The parameters of c_i and n_i were obtained from curve fitting of the experimental data of average plateau stress, plateau slope, and densification limit for each topology studied, which are summarised in Table 6. The average plateau stress was initially defined by Eq. (16); then, the plateau slope is incorporated in the predicted strain-stress response, Eq. (17), which is defined until the densification stress, Eq. (18). The initial elastic stage is neglected, and the theoretical SEA can be extracted from this approach up to the densification point. The same approach was used for quasi-static and impact conditions according to the experimental loading rate.

The theoretical predictions are presented in Fig. 15-17 for all the topologies studies. A good prediction was noted for all the topologies, presenting R^2 between 0.95 and 0.99 and the best prediction observed for Diamond (D) TPMS. Table 7 summarises the SEA obtained from the theoretical models, showing a strain-rate effect in the impact response of all the TPMS-based lattices studied, indicating SEA up to 25% higher than observed in quasi-static compressive tests due to the base material strain-rate sensitivity. Thus, the proposed theoretical modelling considering the strain-rate hardening effect, $\kappa_{\dot{\varepsilon}}$, provides reasonably accurate predictions of the impact strain-stress and SEA of the TPMS-based lattices studied.

The theoretical SEA gives a reasonable prediction of the maximum energy absorption of the lattices under impact up to the densification point for a given topology and relative density, which varies from 21 J/g up to 53 J/g. The SEA increases with the strain-rate and the relative density within the range studied. However, the lattice topologies studied do not strongly influence the resulting SEA.

3.4. Functionally graded lattices

Functionally graded (FG) lattices were proposed to improve the impact performance of the Diamond (D) lattice in terms of SEA and residual deformation after impact (DAI). Eight different gradients were considered, as follows

Linearly Graded 1 (LG1):

$$\rho = 0.20 + 0.0125z, \tag{17}$$

Linearly Graded 2 (LG2):

$$\rho = 0.10 + 0.0250z, \tag{18}$$

Linearly Graded 3 (LG3):

$$\rho = 0.40 - 0.0125z, \tag{19}$$

Linearly Graded 4 (LG4):

$$\rho = 0.50 - 0.0250z, \tag{20}$$

Quadratically Graded 1 (QG1):

$$\rho = 0.50 - 0.075z + 0.0047z^2, \tag{21}$$

Quadratic Graded 2 (QG2):

$$\rho = 0.40 - 0.0375z + 0.00235z^2, \tag{22}$$

Quadratic Graded 3 (QG3):

$$\rho = 0.10 + 0.075z - 0.0047z^2, \tag{23}$$

Quadratic Graded 4 (QG4):

$$\rho = 0.20 + 0.0375z - 0.00235z^2, \tag{24}$$

where z is the vertical position taken from the bottom of the TPMS and ρ

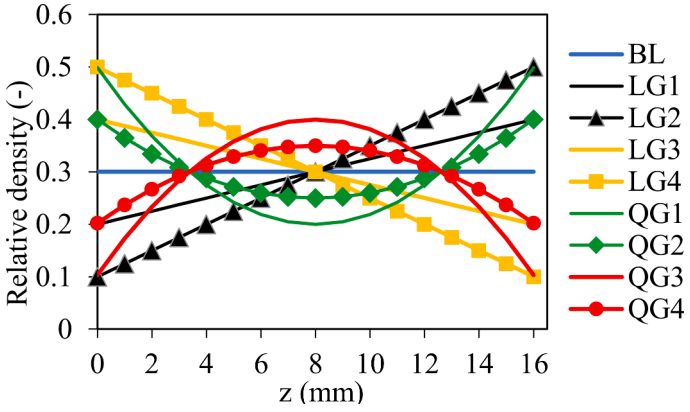

Fig. 21. Relative densities distribution for the functionally graded lattices proposed.

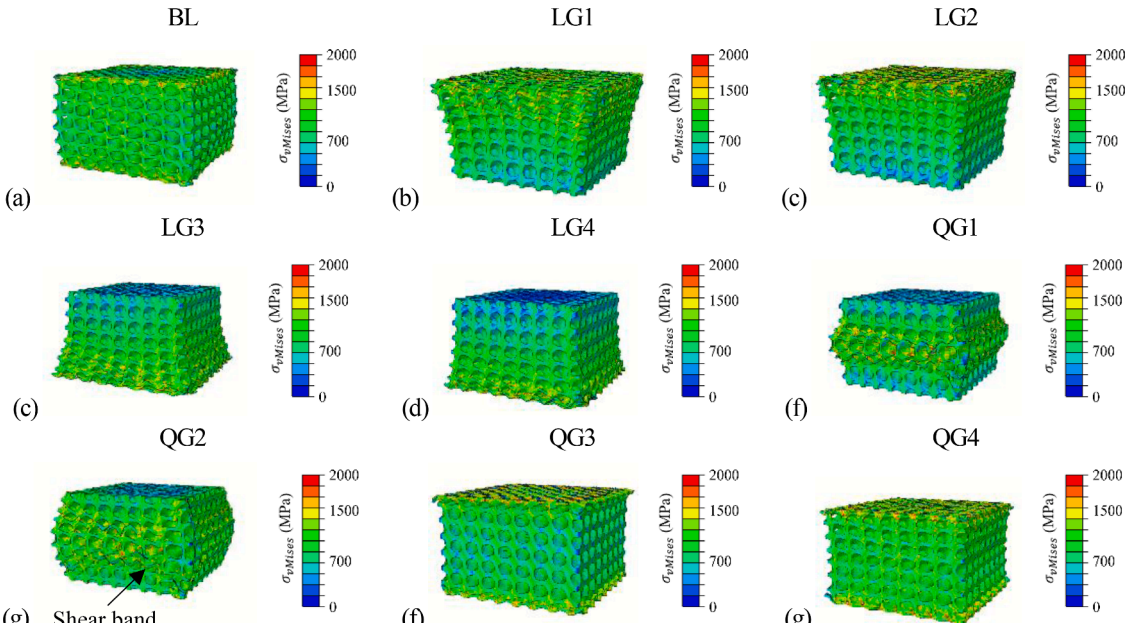

Fig. 22. Graded Diamond TPMS at $\varepsilon = 0.30$ during impact.

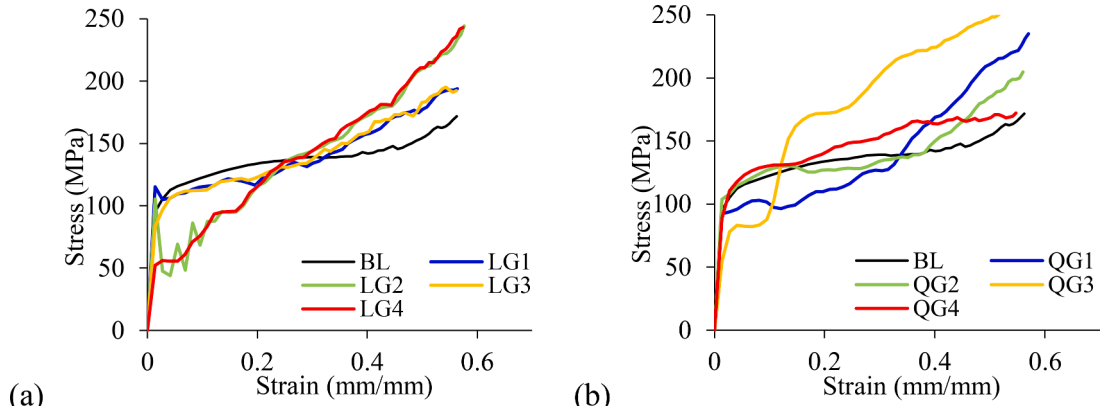

Fig. 23. Compressive stress-strain reponses (a) linearly and (b) quadratically graded D TPMS topologies.

Table 8
Summary of the SEA and DAI for the BL and the functionally graded topologies.

Topology	SEA* (J/g)		DAI (mm/mm)	
BL	27.79	–	0.56	–
QG1	27.05	(-2.7%)	0.57	(+1.3%)
QG2	28.38	(+2.1%)	0.56	(-0.5%)
QG3	36.39	(+31.0%)	0.52	(-8.2%)
QG4	30.70	(+10.5%)	0.53	(-6.6%)
LG1	27.87	(+0.3%)	0.56	(+0.2%)
LG2	27.12	(-2.4%)	0.58	(+2.4%)
LG3	28.40	(+2.2%)	0.56	(-0.1%)
LG4	26.95	(-3.0%)	0.57	(+2.1%)

* : up to $\varepsilon = 0.50$ and $\rho = 30\%$.

is the relative density. All the proposed graded lattices exhibit the same overall relative density of $\overline{\rho} = 30\%$, and a non-graded topology is considered as a baseline (BL). Fig. 21 summarises the relative density distribution through the lattice height.

Fig. 22 compares the behaviour of the BL and graded topologies after impact, clearly showing the changes of deformation modes of lattices due to grading. Meanwhile, the BL deformation is governed by shear-band formation, but the deformation mode of most graded lattices is primarily layer-based, usually triggered by the lowest relative density section. The only exception is QG2, which keeps a shear band deformation mode.

Fig. 23 compares the stress-strain responses for the graded lattices studied. The evident plateau in the BL is also noted in QG2 and QG4, with a roughly similar response. However, a crescent stress-strain response was observed in all the linearly graded lattices (LG1, LG2, LG3 and LG4) and the more severe quadratically graded ones (i.e., QG1 and QG3). In the former case, the higher the gradient, the higher the slope of the stress-strain curve, independent of the relative density gradient direction, as observed in LG1 and LG3 or LG2 and LG4.

Table 8 and Fig. 24 summarise the DAI and SEA, up to $\varepsilon = 0.50$, for the BL and the graded topologies studied. Besides the evident change in the deformation mode and the stress-strain response, the crescent linear functionally graded (e.g. LG1 and LG2), the negative linear functionally graded (LG3 and LG4) and the positive curvature quadratic functionally graded lattices (QG1 and QG2, i.e. higher relative density at the central cube section) exhibit marginal improvements on the impact performance.

However, an improvement of SEA and DAI was noted for the negative curvature quadratic functionally graded lattices (QG3 and QG4). In these lattices, the SEA was improved by 10.5% and 31.0%, and the DAI

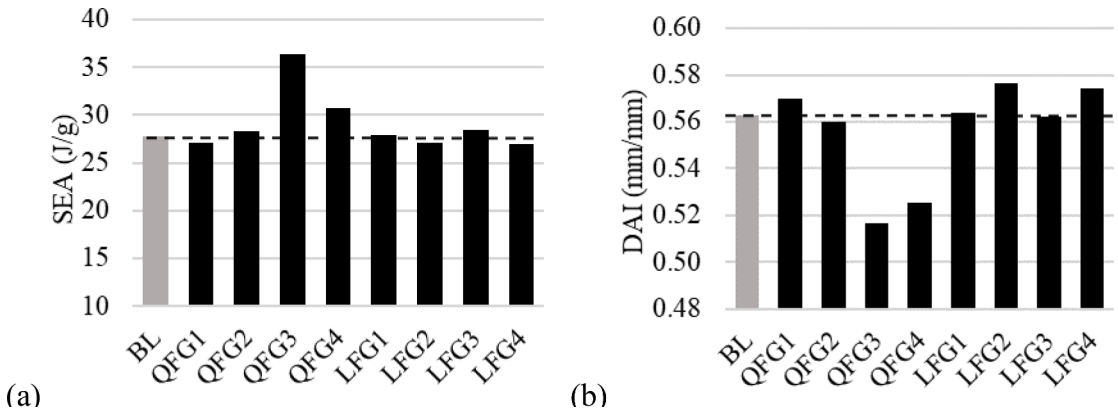

Fig. 24. Comparison of (a) specific energy absorption (SEA) and (b) deformation after impact (DAI) for the BL and the functionally graded topologies. An evident improvement is observed on QFG3 and QFG4, by enhancing the SEA up to 31% and reducing DAI up to 8.1%.

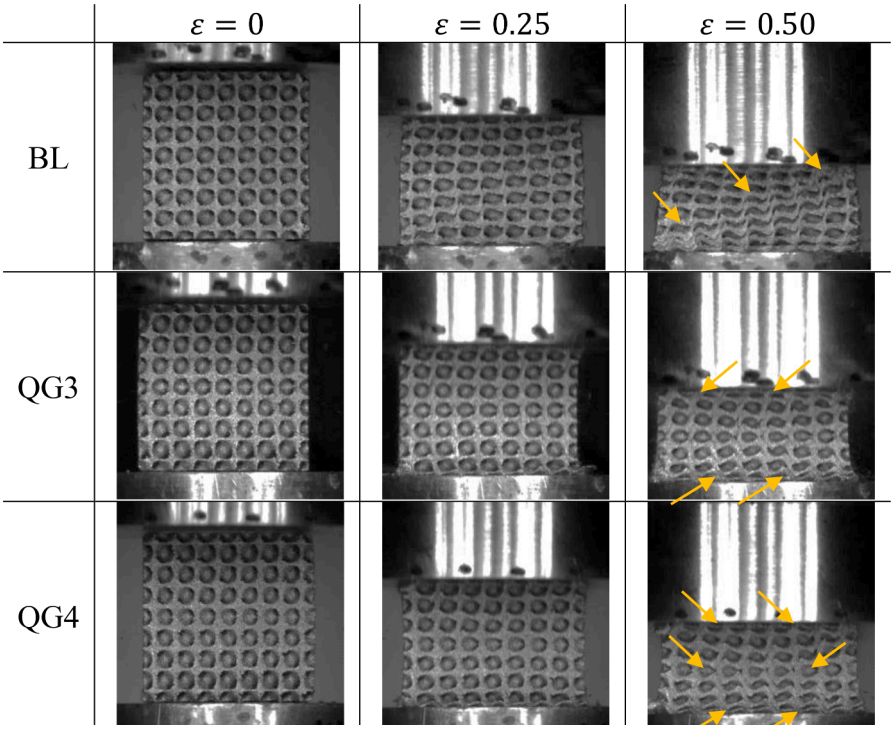

Fig. 25. Evolution of the deformation mode of TPMS lattices during the impact.

was reduced by 6.6% and 8.2%, respectively. It was noted that the graded function increased the relative density of the unit cells located at the central cube section, in which the densification was observed in the BL configuration. Likewise, the relative density of the upper and lower unit cell layers was reduced, which did not exhibit high deformation levels in the non-graded lattice. Therefore, QG3 and QG4 could provide the optimised relative density distribution of the lattices, improving and reducing the lattice stiffness in appropriate locations, resulting in superior impact performance.

It is important to mention that the present graded function is intended to deliver superior performance for a given material, lattice topology and impact conditions explored here. Thus, this work shows a great potential of using graded lattices to improve impact resistance of lattices, particularly for energy absorption applications.

3.5. Experimental verification

BL, QG3, and QG4 topologies were additively manufactured as described in Section 2, with an overall relative density of 36% for all the topologies. Although the topologies described in Section 3.4 were used for manufacturing the lattices, the limitations of the L-PBF technique resulted in slightly higher relative densities.

The topologies were tested under impact in a DIHB device, with the evolution of the deformation exhibited in Fig. 25. It was noted that the deformation mode changed from a shear-band formation in BL to a progressive layer buckling in QG3, due to the lower relative density of the lattice layer at the impact face. In addition, QG4 topology exhibited a mixed deformation mode, with the shear band in its central part and progressive layer buckling at the impact face. The FE modelling in Section 3.4 provided the prediction of the change in the deformation mode, as observed experimentally.

Fig. 26 compares the strain-stress curves of the topologies during impact, indicating the response differences. The BL exhibited a mild hardening plateau stress until the densification, whereas the graded topologies revealed a crescent strain-stress response. Besides this, it was noted that the slope of the strain-stress curve of QG3 is higher than that

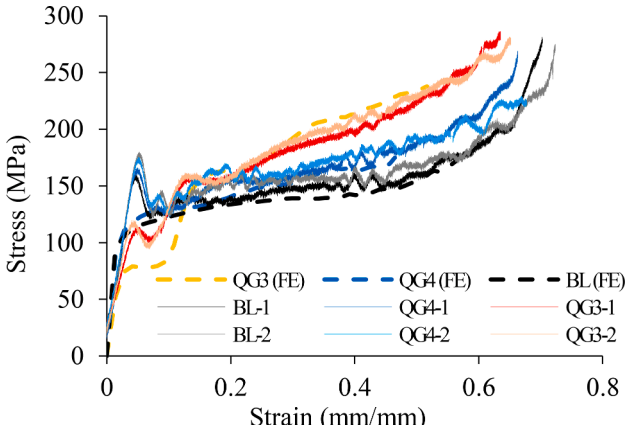

Fig. 26. Strain-stress responses of BL-*n*, QG3-*n* and QG4-*n* topologies during impact, with *n* representing the specimen identification number.

Table 9
Summary of experimental results for BL, QG3 and QG4 topologies.

Topology	SEA* (J/g)		DAI (mm/mm)	
BL	28.55	–	0.73	–
QG3	33.81	(+18.4%)	0.67	(-5.0%)
QG4	30.68	(+7.5%)	0.68	(-8.0%)

* : up to $\varepsilon = 0.50$ and $\rho = 36\%$.

of QG4 lattices. The strain-stress responses corroborate with the FE simulations.

As summarised in Table 9, the SEA values of QG3 and QG4 increased by 18.4% and 7.5%, respectively, compared to BL. Additionally, the DAI values were reduced by 5.0% for QG3 and 8.0% for QG. In general, the predicted increase of the SEA and the decrease of the DAI agree with the experimental results reasonably well, which confirms the enhancement of the impact performance of TPMS-based lattices by using functionally graded topologies. Thus, these characteristics can be used to optimise the impact performance of the components made with the lattice structures subjected to impact loading, such as aircraft wings, automotive crash boxes, helmets and armouring.

4. Conclusions

The present work has been carried out to develop the base material mechanical characterisation and the theoretical and numerical modelling of TPMS-based lattices to improve its impact resistance. The additively manufactured stainless steel 316 L alloy lattices have been mechanically characterised up to a strain-rate of 4000 s^{-1} and at different built-up directions. Anisotropic constitutive parameters were defined and used in an explicit finite element (FE) model. The FE models were validated against the corresponding experimental data for three TPMS topologies subjected to impact velocities up to 33 m/s, with the deviation between numerical and experimental results varying between 2% and 8%.

A theoretical model has also been proposed which provides good predictions of the TPMS behaviour up to the densification at quasi-static and dynamic loadings. Theoretical predictions of the SEA values of TPMS-based lattices suggest that the lattices investigated present the capability to absorb a SEA up to 53 J/g under impact, depending mainly on the relative density. Finally, the validated FE models were used to explore the impact response of functionally graded lattices. Functionally graded lattices were manufactured and verified experimentally, indicating that quadratically functionally graded with negative curvature could improve the SEA up to 18.4% and reduce the displacement after impact up to 8.1% compared to the non-graded counterpart.

The present work highlights the potential of graded lattices for low-velocity impact performance of TPMS-based lattices. Based on the study, the impact resistance of the lattice could be substantially improved by grading the material within the lattice. It is important to mention that the amount of material used, the energy consumed, and the manufacturing cost are kept the same; meanwhile, considerable gains on SEA were observed. Optimised TPMS-based lattices have great potential in defence, aerospace, prosthesis, and automotive applications.

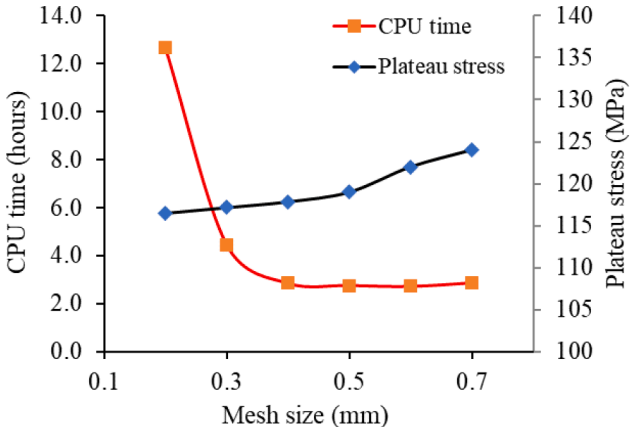

Fig. A1. : Mesh sensitivity analysis.

CRediT authorship contribution statement

Rafael Santiago: Conceptualization, Investigation, Writing – original draft. **Henrique Ramos:** Validation, Investigation. **Sara AlMahri:** Investigation. **Omar Banabila:** Formal analysis, Investigation. **Haleimah Alabdouli:** Formal analysis. **Dong-Wook Lee:** Conceptualization. **Alia Aziz:** Investigation. **Nitul Rajput:** Investigation. **Marcilio Alves:** Supervision. **Zhongwei Guan:** Supervision, Writing – review & editing.

Declaration of Competing Interest

The authors declare that they have no known competing financial interests or personal relationships that could have appeared to influence the work reported in this paper.

Data availability

Data will be made available on request.

Acknowledgements

The authors acknowledge the Advanced Technology Research Council (ATRC), Prof. Wesley Cantwell for providing CT-Images and Natalia Ghisi for supporting with SEM images. Marcilio Alves would like to acknowledge the support of the São Paulo Research Foundation (FAPESP), process 2019-054444-0.

Supplementary materials

Supplementary material associated with this article can be found, in the online version, at doi:10.1016/j.ijimpeng.2023.104592.

Appendix A – Mesh sensitivity analysis

The comparison of numerical plateau stress levels obtained and CPU processing time with varying element mesh size is presented in Fig. 27.

References

[1] Materials for additive manufacturing. Elsevier; 2021. https://doi.org/10.1016/C2018-0-01951-9.

[2] Del Guercio G, Galati M, Saboori A, Fino P, Iuliano L. Microstructure and mechanical performance of Ti–6Al–4V lattice structures manufactured via Electron Beam Melting (EBM): a review. Acta Metall Sin (English Lett 2020;33:183–203. https://doi.org/10.1007/s40195-020-00998-1.

[3] Gibson LJ, Ashby MF. Cellular solids. Cambridge University Press; 1997. https://doi.org/10.1017/CBO9781139878326.

[4] AlMahri S, Santiago R, Lee D, Ramos H, Alabdouli H, Alteneiji M, Guan Z, Cantwell W, Alves M. Evaluation of the dynamic response of triply periodic minimal surfaces subjected to high strain-rate compression. Addit Manuf 2021: 102220. https://doi.org/10.1016/j.addma.2021.102220.

[5] Novak N, Al-Ketan O, Krstulović-Opara L, Rowshan R, Abu Al-Rub RK, Vesenjak M, Ren Z. Quasi-static and dynamic compressive behaviour of sheet TPMS cellular structures. Compos Struct 2021;266:1–10. https://doi.org/10.1016/j.compstruct.2021.113801.

[6] Mines R. Applications for additively manufactured metallic microlattice structures: core materials in beams and panels, energy absorbers (Static and Impact). SpringerBriefs Appl Sci Technol 2019:75–95. https://doi.org/10.1007/978-3-030-15232-1_7.

[7] Smith M, Cantwell WJ, Guan Z. Impact and blast response of lattice materials, in: dyn. lattice mater. Ltd, Chichester, UK: John Wiley & Sons; 2017. p. 155–78. https://doi.org/10.1002/9781118729588.ch7.

[8] Abu Al-Rub RK, Lee D-W, Khan KA, Palazotto AN. Effective anisotropic elastic and plastic yield properties of periodic foams derived from triply periodic Schoen's I-WP minimal surface. J Eng Mech 2020;146:04020030. https://doi.org/10.1061/(asce)em.1943-7889.0001759.

[9] Maskery I, Aboulkhair NT, Aremu AO, Tuck CJ, Ashcroft IA. Compressive failure modes and energy absorption in additively manufactured double gyroid lattices. Addit Manuf 2017;16:24–9. https://doi.org/10.1016/j.addma.2017.04.003.

[10] O'Masta MR, Dong L, St-Pierre L, Wadley HNG, Deshpande VS. The fracture toughness of octet-truss lattices. J Mech Phys Solids 2017;98:271–89. https://doi.org/10.1016/j.jmps.2016.09.009.

[11] Al-Ketan O, Rowshan R, Abu Al-Rub RK. Topology-mechanical property relationship of 3D printed strut, skeletal, and sheet based periodic metallic cellular materials. Addit Manuf 2018;19:167–83. https://doi.org/10.1016/j.addma.2017.12.006.

[12] Xiao L, Song W, Xu X. Experimental study on the collapse behavior of graded Ti-6Al-4V micro-lattice structures printed by selective laser melting under high speed impact. Thin-Walled Struct 2020;155:106970. https://doi.org/10.1016/j.tws.2020.106970.

[13] Tancogne-Dejean T, Spierings AB, Mohr D. Additively-manufactured metallic micro-lattice materials for high specific energy absorption under static and dynamic loading. Acta Mater 2016;116:14–28. https://doi.org/10.1016/j.actamat.2016.05.054.

[14] Li C, Lei H, Liu Y, Zhang X, Xiong J, Zhou H, Fang D. Crushing behavior of multi-layer metal lattice panel fabricated by selective laser melting. Int J Mech Sci 2018; 145:389–99. https://doi.org/10.1016/j.ijmecsci.2018.07.029.

[15] Cao X, Xiao D, Li Y, Wen W, Zhao T, Chen Z, Jiang Y, Fang D. Dynamic compressive behavior of a modified additively manufactured rhombic dodecahedron 316L stainless steel lattice structure. Thin-Walled Struct 2020;148:106586. https://doi.org/10.1016/j.tws.2019.106586.

[16] Bonatti C, Mohr D. Mechanical performance of additively-manufactured anisotropic and isotropic smooth shell-lattice materials: simulations & experiments. J Mech Phys Solids 2019;122:1–26. https://doi.org/10.1016/j.jmps.2018.08.022.

[17] Abou-Ali AM, Al-Ketan O, Lee DW, Rowshan R, Abu Al-Rub RK. Mechanical behavior of polymeric selective laser sintered ligament and sheet based lattices of triply periodic minimal surface architectures. Mater Des 2020;196:109100. https://doi.org/10.1016/j.matdes.2020.109100.

[18] Zhang L, Feih S, Daynes S, Chang S, Wang MY, Wei J, Lu WF. Energy absorption characteristics of metallic triply periodic minimal surface sheet structures under compressive loading. Addit Manuf 2018;23:505–15. https://doi.org/10.1016/j.addma.2018.08.007.

[19] Abueidda DW, Elhebeary M, (Andrew) Shiang CS, Pang S, Abu Al-Rub RK, Jasiuk IM. Mechanical properties of 3D printed polymeric Gyroid cellular structures: experimental and finite element study. Mater Des 2019;165:107597. https://doi.org/10.1016/j.matdes.2019.107597.

[20] Balabanov SV, Makogon AI, Sychov MM, Gravit MV, Kurakin MK. Mechanical properties of 3D printed cellular structures with topology of triply periodic minimal surfaces. Mater Today Proc 2019;30:439–42. https://doi.org/10.1016/j.matpr.2019.12.392.

[21] Ma S, Tang Q, Han X, Feng Q, Song J, Setchi R, Liu Y, Liu Y, Goulas A, Engstrøm DS, Tse YY, Zhen N. Manufacturability, mechanical properties, mass-transport properties and biocompatibility of triply periodic minimal surface (TPMS) porous scaffolds fabricated by selective laser melting. Mater Des 2020:195. https://doi.org/10.1016/j.matdes.2020.109034.

[22] Altamimi S, Lee D-W, Barsoum I, Rowshan R, Jasiuk IM, Abu Al-Rub RK. On stiffness, strength, anisotropy, and buckling of 30 strut-based lattices with cubic crystal structures. Adv Eng Mater 2022:2101379. https://doi.org/10.1002/adem.202101379.

[23] Krishnan K, Lee D-W, Al Teneji M, Abu Al-Rub RK. Effective stiffness, strength, buckling and anisotropy of foams based on nine unique triple periodic minimal surfaces. Int J Solids Struct 2022;238:111418. https://doi.org/10.1016/j.ijsolstr.2021.111418.

[24] Khrapov D, Koptyug A, Manabaev K, Léonard F, Mishurova T, Bruno G, Cheneler D, Loza K, Epple M, Surmenev R, Surmeneva M. The impact of post manufacturing treatment of functionally graded Ti6Al4V scaffolds on their surface morphology and mechanical strength. J Mater Res Technol 2020;9:1866–81. https://doi.org/10.1016/j.jmrt.2019.12.019.

[25] Lei H, Li C, Zhang X, Wang P, Zhou H, Zhao Z, Fang D. Deformation behavior of heterogeneous multi-morphology lattice core hybrid structures. Addit Manuf 2021; 37:101674. https://doi.org/10.1016/j.addma.2020.101674.

[26] Smith M, Guan Z, Cantwell WJ. Finite element modelling of the compressive response of lattice structures manufactured using the selective laser melting technique. Int J Mech Sci 2013;67:28–41. https://doi.org/10.1016/j.ijmecsci.2012.12.004.

[27] Zhao M, Zhang DZ, Liu F, Li Z, Ma Z, Ren Z. Mechanical and energy absorption characteristics of additively manufactured functionally graded sheet lattice structures with minimal surfaces. Int J Mech Sci 2020:167. https://doi.org/10.1016/j.ijmecsci.2019.105262.

[28] Wang Y, Ren X, Chen Z, Jiang Y, Cao X, Fang S, Zhao T, Li Y, Fang D. Numerical and experimental studies on compressive behavior of Gyroid lattice cylindrical shells. Mater Des 2020;186:108340. https://doi.org/10.1016/j.matdes.2019.108340.

[29] Li X, Roth CC, Tancogne-Dejean T, Mohr D. Rate- and temperature-dependent plasticity of additively manufactured stainless steel 316L: characterization, modeling and application to crushing of shell-lattices. Int J Impact Eng 2020;145: 103671. https://doi.org/10.1016/j.ijimpeng.2020.103671.

[30] Peng C, Tran P. Bioinspired functionally graded gyroid sandwich panel subjected to impulsive loadings. Compos Part B Eng 2020;188:107773. https://doi.org/10.1016/j.compositesb.2020.107773.

[31] Ramos H, Santiago R, Soe S, Theobald P, Alves M. Response of gyroid lattice structures to impact loads. Int J Impact Eng 2022:104202. https://doi.org/10.1016/j.ijimpeng.2022.104202.

[32] Classic Split-Hopkinson Pressure Bar Testing. Mech. test. eval. ASM International; 2000. p. 462–76. https://doi.org/10.31399/asm.hb.v08.a0003296.

[33] Chen W, Song B. Split hopkinson (Kolsky) bar. Boston, MA: Springer US; 2011. https://doi.org/10.1007/978-1-4419-7982-7.

[34] Kariem MA, Santiago RC, Govender R, Shu DW, Ruan D, Nurick G, Alves M, Lu G, Langdon GS. Round-Robin test of split Hopkinson pressure bar. Int J Impact Eng 2019;126:62–75. https://doi.org/10.1016/j.ijimpeng.2018.12.003.

[35] ASTM E8. ASTM E8/E8M standard test methods for tension testing of metallic materials 1. Annu B ASTM Stand 2010;4:1–27. https://doi.org/10.1520/E0008.

[36] Schreier H, Orteu J-J, Sutton MA. Image correlation for shape, motion and deformation measurements. Boston, MA: Springer US; 2009. https://doi.org/10.1007/978-0-387-78747-3.

[37] Buehler. Buehler® summettm - A Guide to materials preparation and analysis. 4th editio. Lake Bluff: Buehler; 2018.

[38] M. Alves, Impact engineering: fundamentals, experiments and nonlinear finite elements, Editora Cubo, 2020. https://doi.org/10.4322/978-85-455210-0-6.

[39] Abueidda DW, Abu Al-Rub RK, Dalaq AS, Lee DW, Khan KA, Jasiuk I. Effective conductivities and elastic moduli of novel foams with triply periodic minimal surfaces. Mech Mater 2016;95:102–15. https://doi.org/10.1016/j.mechmat.2016.01.004.

[40] Andrews EW, Gioux G, Onck P, Gibson LJ. Size effects in ductile cellular solids. Part II: experimental results. Int J Mech Sci 2001;43:701–13. https://doi.org/10.1016/S0020-7403(00)00043-6.

[41] Diebels S, Steeb H. The size effect in foams and its theoretical and numerical investigation. Proc. R. Soc. London. Ser. A Math. Phys. Eng. Sci. 2002;458: 2869–83. https://doi.org/10.1098/rspa.2002.0991.

[42] Y. Shi, C. Yan, Y. Zhou, J. Wu, Y. Wang, S. Yu, Y. Chen, eds., Copyright, in: Mater Addit Manuf, Academic Press, 2021: p. iv. https://doi.org/10.1016/B978-0-12-819302-0.00010-9.

[43] Wang Z, Wang X, Gao T, Shi C. Mechanical behavior and deformation mechanism of triply periodic minimal surface sheet under compressive loading. Mech Adv Mater Struct 2021;28:2057–69. https://doi.org/10.1080/15376494.2020.1829756.

[44] M. Smith, ABAQUS User's Manual, Version 6.14, dassault systèmes simulia corp, United States, 2014.

[45] Hill Rodney. A theory of the yielding and plastic flow of anisotropic metals. Proc R Soc London Ser A Math Phys Sci 1948;193:281–97. https://doi.org/10.1098/rspa.1948.0045.

[46] Sivam SPSS. Frequently used anisotropic yield criteria for sheet metal applications: a review. Indian J Sci Technol 2016;9:1–6. https://doi.org/10.17485/ijst/2016/v9i47/92107.

[47] Neto DM, Oliveira MC, Alves JL, Menezes LF. Influence of the plastic anisotropy modelling in the reverse deep drawing process simulation. Mater Des 2014;60: 368–79. https://doi.org/10.1016/j.matdes.2014.04.008.

[48] Jweeg MJ, Mohammed AI, Jabbar MS. Four Earing's prediction in deep drawing of AISI 1008 steel sheet conical product. IOP Conf Ser Mater Sci Eng 2020:881. https://doi.org/10.1088/1757-899X/881/1/012051.

[49] Johnson GR, Cook WH. Fracture characteristics of three metals subjected to various strains, strain rates, temperatures and pressures. Eng Fract Mech 1985;21:31–48. https://doi.org/10.1016/0013-7944(85)90052-9.

[50] Murugesan M, Jung DW. Johnson cook material and failure model parameters estimation of AISI-1045 medium carbon steel for metal forming applications. Materials (Basel) 2019;12. https://doi.org/10.3390/ma12040609.

[51] Liu J, Pattofatto S, Fang D, Lu F, Zhao H. Impact strength enhancement of aluminum tetrahedral lattice truss core structures. Int J Impact Eng 2015;79:3–13. https://doi.org/10.1016/j.ijimpeng.2014.06.013.
[52] Wang H, Tan D, Liu Z, Yin H, Wen G. On crashworthiness of novel porous structure based on composite TPMS structures. Eng Struct 2022;252:113640. https://doi.org/10.1016/j.engstruct.2021.113640.
[53] Wang X, Muñiz-Lerma JA, Attarian Shandiz M, Sanchez-Mata O, Brochu M. Crystallographic-orientation-dependent tensile behaviours of stainless steel 316L fabricated by laser powder bed fusion. Mater Sci Eng A. 2019;766:138395. https://doi.org/10.1016/j.msea.2019.138395.
[54] Sun Z, Tan X, Tor SB, Chua CK. Simultaneously enhanced strength and ductility for 3D-printed stainless steel 316L by selective laser melting. NPG Asia Mater 2018;10:127–36. https://doi.org/10.1038/s41427-018-0018-5.
[55] Ma M, Wang Z, Zeng X. A comparison on metallurgical behaviors of 316L stainless steel by selective laser melting and laser cladding deposition. Mater. Sci. Eng. A. 2017;685:265–73. https://doi.org/10.1016/j.msea.2016.12.112.